We would like to thank the editor and reviewers for their helpful comments that improved this manuscript. Below in *italics* please, find our replies to the Reviewer #1 and editor's comments and suggested changes.

Reviewer #1 comments: In the revised version of the manuscript, the authors have added more comparisons between the old and the new data product and fixed a number of smaller issues. This has in my opinion significantly improved the manuscript, which now is fit for publication. I still find it disappointing that no case could be shown where the new data product is clearly superior to the old one in the sense of more realistic or more consistent tropospheric NO2 columns. I also don't understand why the authors do not add V3.1 results in Table 2 - readers will be interested to know how the agreement to the validation data changed. In my opinion, this information should still be added before publication.

Editor's comments: I consider the manuscript to be almost ready for publication, but there is one small remaining point raised by referee #1, which I would like you to reconsider: The referee would have liked to see also results from V3.1 in Table 2 and argues that readers (and users of the new product) will be interested to know how the agreement with the validation data changed.

We realize that inclusion of results from V3.1 in Table 2 would allow an easy assessment of validation results, although some of these V3.1-related results were already published in our previous work by Choi et al., (2020) as we clarified in our earlier response. We now include corresponding results from V3.1. For clarity, we split the results presented in Table 2 into two tables (Table 2 and 3), with Table 2 showing the comparison of OMI V3.1 and V4.0 with the P-3B aircraft observations and Table 3 showing the comparison with Pandora observations. We have also made necessary changes in the text in Section 3.2.

Reviewer #1 comments: The authors also may want to check line 747 for a small editing issue. *Thanks. The typographical error is corrected.*

OMI/Aura Nitrogen Dioxide Standard Product Version 4.0 with Improved Surface and Cloud Treatments

Lok N. Lamsal *[,1,2], Nickolay A. Krotkov[2], Alexander Vasilkov[2,3], Sergey Marchenko[2,3], Wenhan Qin[2,3], Eun-Su Yang[2,3], Zachary Fasnacht[2,3], Joanna Joiner[2], Sungyeon Choi[2,3], David Haffner[2,3], William H. Swartz[4], Bradford Fisher[2,3], Eric Bucsela[5]

[1]University Space Research Association, Greenbelt, MD 20770, USA

[2]NASA Goddard Space Flight Center, Greenbelt, MD 20770, USA

[3]Science Systems and Applications, Lanham, MD 20706, USA

[4]Johns Hopkins University, Applied Physics Laboratory, Laurel, MD 20723, USA

[5]SRI International, Menlo Park, CA 94025, USA

*Corresponding author: Email: lok.lamsal@nasa.gov.

18   **Abstract**

19   We present a new and improved version (V4.0) of the NASA standard nitrogen dioxide (NO_2)
20   product from the Ozone Monitoring Instrument (OMI) on the Aura satellite. This version
21   incorporates the most salient improvements for OMI NO_2 products suggested by expert users and
22   enhances the NO_2 data quality in several ways through improvements to the air mass factors
23   (AMFs) used in the retrieval algorithm. The algorithm is based on geometry-dependent surface
24   Lambertian equivalent reflectivity (GLER) operational product that is available on an OMI pixel
25   basis. GLER is calculated using the vector linearized discrete ordinate radiative transfer
26   (VLIDORT) model, which uses as input high resolution bidirectional reflectance distribution
27   function (BRDF) information from NASA's Aqua Moderate Resolution Imaging
28   Spectroradiometer (MODIS) instruments over land and the wind-dependent Cox–Munk wave-
29   facet slope distribution over water, the latter with contribution from the water-leaving radiance.
30   The GLER combined with consistently retrieved oxygen dimer (O_2-O_2) absorption-based effective
31   cloud fraction (ECF) and optical centroid pressure (OCP) provide improved information to the
32   new NO_2 AMF calculations. The new AMFs increase the retrieved tropospheric NO_2 by up to 50%
33   in highly polluted areas; these differences arise from both cloud and surface BRDF effects as well
34   as biases between the new MODIS-based and previously used OMI-based climatological surface
35   reflectance data sets. We quantitatively evaluate the new NO_2 product using independent
36   observations from ground-based and airborne instruments. The new V4.0 data and relevant
37   explanatory documentation are publicly available from the NASA Goddard Earth Sciences Data
38   and Information Services Center (https://disc.gsfc.nasa.gov/datasets/OMNO2_V003/summary/),
39   and we encourage their use over previous versions of OMI NO_2 products.

Introduction

The Dutch/Finnish-built Ozone Monitoring Instrument (OMI) has been operating on board the NASA EOS-Aura spacecraft since July 2004 (Levelt et al., 2006, 2018). The primary objectives of OMI's mission are to continue the long-term record of total column ozone and to monitor other trace gases relevant to tropospheric pollution worldwide. Observations of sunlight backscattered from the Earth over a wide range of UV and visible wavelengths (~260-500 nm) made by OMI allow for the retrieval of various atmospheric trace gases, including nitrogen dioxide (NO_2). NO_2 is a critically important short-lived air pollutant originating from both anthropogenic and natural sources. It is the principal precursor to tropospheric ozone and a key agent for the formation of several toxic airborne substances such as nitric acid (HNO_3), nitrate aerosols, and peroxyacetyl nitrate. Satellite-based observations yield a global, self-consistent NO_2 data record that can complement field measurements.

During more than 16 years of operation, OMI has provided a unique, practically uninterrupted daily NO_2 data record that has been widely used for atmospheric research and applications, accentuating demands for accurate NO_2 data products. The power of OMI to track NO_2 pollution is demonstrated through observations of enhanced column amounts over polluted industrial areas (*e.g.*, Boersma et al., 2011; Lamsal et al., 2013; Krotkov et al., 2016; Kim et al., 2016; Cai et al., 2018; Montgomery and Halloway, 2018), weekly patterns with significant reduction on weekends following energy usage (*e.g*., Ialongo et al., 2016), and seasonal patterns (e.g., van der A et al., 2008) that reflect changes in NO_x emissions and photochemistry (*e.g*., Shah et al., 2019). Exploiting the close relationship between NO_x emissions and tropospheric NO_2 columns, OMI NO_2 data have been used to detect and quantify the strength and trends of NO_x emissions from power plants (Duncan et al., 2013; de Foy *et al.*, 2015; Liu et al., 2019), ships (*e.g*., Vinken et al., 2014a), lightning (*e.g*., Picketing et al., 2016), soil (*e.g*., Vinken et al., 2014b), oil and gas production (e.g., Dix et al., 2020), forest fires (Schreier et al, 2014), and other area sources such as cities in the US (Lamsal *et al.,* 2015; Lu *et al.,* 2015; Kim et al., 2016), Europe (*e.g*., Zhou et al., 2012; Castellanos et al., 2012; Vinken et al., 14a), Asia (Ghude et al., 2013; Goldberg et al., 2019a), and other world urban areas (Krotkov *et al.,* 2016; Duncan *et al*., 2016; Montgomery and Halloway, 2018). OMI NO_2 observations have frequently seen used to evaluate chemical transport models (CTMs) (*e.g*., Herron-Thrope et al., 2010; Han et al., 2011; Hudman et al., 2012; Pope et al., 2015; Rasool et al., 2016), to study atmospheric NO_x chemistry and lifetime (*e.g*., Lamsal et

71 al., 2010; Beirle et al., 2011; Canty et al., 2015; Tang et al., 2015; Laughner and Cohen, 2019),

72 and to infer ground-level NO_2 concentrations (Lamsal et al., 2008; Gu et al., 2017), NO_2 dry

73 deposition (Nowlan et al., 2014, Geddes and Martin, 2017), and emissions of co-emitted gases

74 including carbon dioxide (CO_2) (Konovalov et al., 2016; Goldberg et al., 2019b, Liu et al., 2019).

75 Over the last decade, there have been considerable efforts to improve NO_2 data quality from OMI

76 and other satellite instruments (e.g., Boersma et al., 2018). A special emphasis has been placed on

77 improving auxiliary information (e.g., a priori NO_2 vertical profiles, surface reflectivity),

78 particularly with respect to spatial and temporal resolution. For instance, the global OMI NO_2

79 products are based on a priori NO_2 profiles from relatively coarse-resolution (>1.0°× 1.25°) global

80 CTM simulations (Boersma et al., 2011; Krotkov et al., 2017, Choi et al., 2020). Many regional

81 studies suggest a general low-bias in the global tropospheric NO_2 column products, particularly

82 over polluted areas, that can be partially mitigated by using a-priori information from high-

83 resolution CTM simulations (Russell et al., 2011, McLinden et al., 2014; Lin et al., 2014; 2015;

84 Goldberg et al., 2018; Choi et al., 2020). Current global NO_2 retrievals are based on a low-

85 resolution (0.5°× 0.5°) static climatology of surface Lambert-Equivalent Reflectivity (OMLER)

86 product (Kleipool et al., 2008), which is likely biased high due to insufficient cloud and aerosol

87 screening. This bias in surface reflectivity can lead to an underestimation of tropospheric NO_2

88 retrievals (Zhou et al., 2010; Lin et al., 2014; Vasilkov et al., 2017). In addition, the OMLER data

89 do not account for the significant day-to-day (orbital) variability in surface reflectance caused by

90 changes in sun-satellite geometry, a phenomenon often expressed by the bi-directional reflectance

91 distribution function (BRDF). Zhou et al. (2010) demonstrated the impact of both the spatial

92 resolution and the BRDF effect on OMI tropospheric NO_2 retrievals over Europe by using high-

93 resolution surface BRDF and albedo products from the Moderate Resolution Imaging

94 Spectroradiometer (MODIS). Taking advantage of the MODIS high resolution data, albeit

95 neglecting the BRDF and atmospheric effects, Russell et al (2011) and McLinden et al (2014)

96 created improved NO_2 products from the NASA Standard Product (Bucsela et al., 2013; Lamsal

97 et al., 2014) over the continental US and Canada, respectively. While these and subsequent studies

98 (e.g., Kuhlmann et al., 2015; Laughner et al., 2019) addressed the limitation of climatological LER

99 data on NO_2 retrievals, they did not account for the surface BRDF effect on the OMI cloud products

100 (cloud pressure/fraction), which are also inputs to the NO_2 algorithm. Applying the MODIS BRDF

101 data consistently to both the NO_2 and cloud retrievals demonstrably improves the quality of OMI

102 NO$_2$ retrievals over China (Lin et al., 2014, 2015, Liu et al., 2019). However, this approach is
103 computationally expensive and is applicable to land surfaces only. Our previous work (Vasilkov
104 et al., 2018) proposed an approach appropriate for satellite NO$_2$ data processing on a global scale
105 (a) by using MODIS BRDF information consistently in the cloud and NO$_2$ retrievals; (b) for both
106 land and water; and (c) in an efficient way. Here, we apply the approach globally for the first time
107 in the standard NASA OMI NO$_2$ algorithm.

108 In this paper we describe various updates made in the version 4.0 (V4.0) NASA OMI NO$_2$
109 algorithm, discuss their impact on the retrievals of tropospheric and stratospheric NO$_2$ column
110 amounts, and provide an initial quantitative assessment of NO$_2$ data quality. Section 2 describes
111 the OMI NO$_2$ algorithm and various auxiliary data used by the algorithm. We present validation
112 results in Section 3. Section 4 summarizes the conclusions of this study.

113 **2 OMI and the NO$_2$ Standard Product**

114 OMI is a ultraviolet-visible (UV-Vis) spectrometer on the polar-orbiting NASA Aura satellite
115 (Levelt et al., 2006, 2018). Aura, launched on July 15, 2004, follows a sun-synchronous orbit with
116 an equator crossing time near 13:45 local time. OMI employs two-dimensional CCD detectors and
117 operates in a push-broom mode, registering spectral data over a 2600 km cross-track spatial swath.
118 The broad swath enables global daily coverage within 14-15 orbits. In the OMI visible channel
119 used for NO$_2$ retrievals, each swath, measured every two seconds, comprises 60 cross-track fields
120 of view (FOVs) varying in size from ~13 km × 24 km near nadir to ~24 km × 160 km for the FOVs
121 at the outermost edges of the swath. Each orbit consists of ~1650 swaths from terminator to
122 terminator. OMI's full daily coverage has been affected by data loss due to an anomaly presumably
123 caused by material on the spacecraft outside the instrument that results in reduced coverage to
124 about half of its original swath as discussed in Section 2.4.

125 The OMI NO$_2$ Standard Product (OMNO2) algorithm provides retrievals of NO$_2$ column (total,
126 tropospheric, and stratospheric) amounts by exploiting Level-1B calibrated radiance and irradiance
127 data from the Vis channel (350-500 nm with 0.63 nm spectral resolution). The algorithm employs
128 a multi-step procedure that consists of 1) a spectral fitting algorithm to calculate NO$_2$ slant column
129 densities (SCDs) as discussed in Section 2.1; 2) determination of air mass factors (AMFs) to
130 convert SCDs to vertical column densities (VCDs) as discussed in detail in Section 2.2; 3) a
131 scheme to remove cross-track dependent artifacts or stripes; and 4) a stratosphere-troposphere
132 separation scheme to derive tropospheric and stratospheric NO$_2$ VCDs. The AMF depends upon a

133 number of parameters including optical geometry (solar and viewing azimuth and zenith angles),

134 surface reflectivity, cloud pressure and fraction, and the shape of the NO_2 a priori vertical profile.

135 Since the first release of OMNO2 in 2006 (Bucsela et al., 2006; Celarier et al., 2008), there have

136 been significant conceptual and technical improvements in the retrieval of NO_2 from space-based

137 measurements. Prior versions developed a new scheme for separating stratospheric and

138 tropospheric components in version 2.1 (V2.1) (Bucsela et al., 2013, Lamsal et al., 2014) and a

139 new algorithm for improved NO_2 SCD retrievals in V3.0 (Marchenko et al., 2015, Krotkov et al.,

140 2017), and included improved cloud products (Veefkind et al., 2016) in V3.1 (Choi et al., 2020).

141 The current version, V4.0, further improves on the retrievals in a number of significant ways for

142 NO_2 AMF and VCD calculations. Figure 1 shows a schematic diagram of the retrieval algorithm,

143 and Table 1 summarizes the differences and similarities between previous (V3.1) and current (V4)

144 versions. Some of the approaches in the V4 algorithm are similar to those used in V3.1, but there

145 are several important changes as discussed in detail in Sections 2.1 and 2.2.

146 **2.1 NO_2 and O_2-O_2 spectral fitting**

147 **2.1.1 NO_2 spectral fitting algorithm**

148 The spectral fitting algorithm for the operational standard OMI NO_2 product is described in detail

149 in Marchenko et al. (2015). Briefly, the algorithm retrieves NO_2 slant column densities (SCDs) by

150 using a Differential Optical Absorption Spectroscopy (DOAS) approach (e.g., Platt and Stutz,

151 2006). In the DOAS approach, laboratory-measured spectra of NO_2 (Vandaele et al., 1998) and

152 glyoxal (Volkamer et al., 2005), HITRAN08-based water vapor spectra (Rothman et al., 2009),

153 and rotational Raman (RR; Ring effect) filling-in are sequentially fitted to the OMI-measured

154 reflectance spectrum in the 402-465 nm wavelength range. The slant column represents the

155 integrated abundance of NO_2 along the average photon path from the Sun, through the atmosphere,

156 to the satellite. The Ring spectra are calculated as a linear combination of the atmospheric (Joiner

157 et al. 1995) and the liquid-water (Vasilkov et al., 2002) RR spectra, convolved with the wavelength

158 and cross-track dependent OMI transfer function (Dirksen et al., 2006). The algorithm employs a

159 multi-step, iterative retrieval procedure for removal of the Ring and spectral under-sampling

160 (Chance, et al., 2005) patterns as well as a low-order polynomial smoothing prior to estimation of

161 SCDs for all interfering species. This is in contrast with the conventional DOAS approach that

162 treats the Ring effect as a pseudo-absorber and fits all absorbers simultaneously with the

163 polynomial functions. For accurate wavelength shifts (radiances vs. irradiances), the standard
164 product algorithm splits the entire fitting window into seven carefully selected, partially
165 overlapping micro-windows, iteratively evaluates the RR spectrum amplitudes, performs
166 wavelength adjustments for each segment, and then iteratively retrieves the NO_2, H_2O, and glyoxal
167 in the windows best suited for a particular trace-gas species.

168 The OMI NO_2 SCDs from the standard product were compared with improved SCD retrievals
169 from the Quality Assurance for Essential Climate Variables (QA4ECV, http://www.qa4ecv.eu/),
170 BIRA-IASB's (Royal Belgian Institute for Space Aeronomy) QDOAS software (http://uv-
171 vis.aeronomie.be/software/QDOAS/), and the latest KNMI retrievals (van Geffen et al., 2015) and
172 are shown to agree within 2% (Zara et al., 2018). The typical NO_2 SCD uncertainties amount to
173 ~0.8×10^{15} molec cm^{-2}, or 5-7% in high-SCD areas and 15-20% in low-SCD values (Marchenko et
174 al., 2015).

175 **2.1.2 O_2-O_2 spectral fitting algorithm**

176 The oxygen dimer (O_2-O_2) slant column fitting algorithm shares many features of the NO_2 fitting
177 algorithm and is described in detail in Vasilkov et al. (2018). It consists of a multi-step, iterative
178 retrieval approach with three carefully selected micro-windows sampling the flanks and the core
179 of the broad O_2-O_2 feature centered at 477 nm. The algorithm exploits OMI-measured reflectance
180 spectra in the 451-496 nm range to determine the wavelength shifts and RR amplitudes. The Ring
181 patterns are removed from the original OMI reflectances during the iterative adjustments for
182 differences in the wavelength registration of radiances and irradiances. The O_2-O_2 slant columns
183 are retrieved after removal of the NO_2 and H_2O absorptions estimated by the algorithm discussed
184 in the previous section, and of the ozone absorption using total ozone data from Veefkind et al.
185 (2006). After removal of the interfering signals, the 477 nm O_2-O_2 absorption profile is carefully
186 normalized to the adjacent O_2-O_2 absorption-free reflectance levels accounting for very different
187 wavelength dependencies of surface reflectances over various geographical sites (e.g., the open-
188 ocean and desert area), as described in Vasilkov et al. (2018). The normalized O_2-O_2 absorption
189 profiles are then iteratively fitted with the temperature-dependent cross-sections from Thalman
190 and Volkamer (2013) over the 463-488 nm range to derive O_2-O_2 SCDs. These are used to estimate
191 the cloud properties as discussed below in Section 2.2.2.

2.2 Improved air mass factor calculations

The AMF, which is defined as the ratio of SCD to VCD, is needed to calculate the retrieved NO_2 VCD. Details of the AMF and its calculation are given in Palmer et al. (2001). The AMF for each FOV is calculated by combining altitude (z)-dependent scattering weights (w) computed with a radiative transfer model and a local a priori vertical NO_2 profile shape (S), taken from a chemistry-transport model:

$$AMF = \int_{z_1}^{z_2} w(z)S(z)dz. \tag{1}$$

For the tropospheric AMF, the integral extends from the surface to the tropopause, whereas the integral from the tropopause to the top of the atmosphere provides the stratospheric AMF. The scattering weight at a given altitude describes the sensitivity of the backscattered radiation to the abundance of the absorber at that altitude. For an optically thin absorber like NO_2, scattering weights are a function of atmospheric scattering and are considered to be independent of the species' vertical distribution (Palmer et al., 2001). Factors affecting scattering weights include wavelength, optical geometry (solar and viewing azimuth and zenith angles), surface reflectivity, and cloud pressure and fraction. The wavelength dependence of scattering weights is accounted for by creating an average of scattering weights derived from the values at multiple wavelengths within the NO_2 spectral fitting window. To compensate for the effect of the assumed constant NO_2 temperature (220 K) in the NO_2 SCD retrievals, the scattering weights are corrected for the atmospheric temperature effect using local climatological monthly temperature profiles as discussed in Bucsela et al. (2013). These profiles are based on the meteorological field from the Modern-Era Retrospective Analysis for Research and Applications (MERRA-2) (Gelaro et al., 2017).

The a priori NO_2 profile shapes are computed from a monthly mean climatology of vertical NO_2 profiles constructed from the Global Modeling Initiative (GMI) CTM simulation (Douglass et al. 2004, Strahan et al., 2007, Strode et al., 2015) driven by MERRA-2 meteorology. The spatial resolution of the model is 1.25° in longitude and 1.0° in latitude, and the atmosphere is divided into 72 pressure levels extending from the surface to 0.01 hPa. The model output is sampled between 13:00 - 14:00, local time, consistent with the OMI overpass time. The use of monthly NO_2 profiles helps capture the seasonal variation in the NO_2 vertical distribution (Lamsal et al., 2010). The simulation is based on yearly varying NO_x emissions, as discussed in Strode et al., (2015); this is necessary to account for the effect of rapidly changing NO_x emissions (e.g., Tong

223   et al., 2015; Duncan et al., 2016; Miyazaki et al., 2017) on local NO_2 profile shapes (Lamsal et al.,

224   2015; Krotkov et al., 2017).

225   For each FOV, AMFs are computed for clear (AMF_{clr}) and cloudy (AMF_{cld}) conditions. The AMF

226   of a partially cloudy scene is calculated by assuming the independent pixel approximation:

227         $AMF = (1 - f_r) \times AMF_{clr} + f_r \times AMF_{cld},$ (2)

228   where f_r is the cloud radiance fraction (CRF), defined as the fraction of the measured radiation

229   that comes from clouds and scattering aerosols, and is computed at 440 nm from the retrieved

230   effective cloud fraction (ECF), f_c using Equation 8 (see below). AMF_{clr} is calculated for the

231   ground reflectivity of R_s and at terrain pressure P_s, whereas AMF_{cld} is calculated assuming a

232   Lambertian surface of reflectivity 0.8 at the retrieved cloud pressure. Below we provide a detailed

233   discussion of each of these input parameters that are incorporated in the OMNO2 V4.0 algorithm.

234   **2.2.1 New surface reflectivity product for NO_2 and cloud retrievals**

235   Surface reflectivity is an important input parameter for UV/Vis satellite retrievals of trace gases

236   and cloud information. The surface reflectance over both ocean and land depend upon viewing and

237   illumination geometry and can be accurately described by the bidirectional reflectance distribution

238   function (BRDF). This effect is, however, neglected by most currently available trace gas and

239   cloud algorithms which use a climatological Lambert-equivalent reflectivity (LER) for the surface.

240   To account for surface BRDF effects in the NO_2 and cloud retrievals, here we use the geometry-

241   dependent surface LER (GLER) product derived using the Moderate Resolution Imaging

242   Spectroradiometer (MODIS) BRDF data and the Vector Linearized Discrete Ordinate Radiative

243   Transfer (VLIDORT) calculation (Vasilkov et al., 2017; Qin et al., 2019; Fasnacht et al., 2019).

244   The GLER allows for a computationally efficient approach that does not require major changes to

245   the existing trace gas and cloud algorithms.

246   We derive GLER by inverting the top-of-atmosphere (TOA) radiance (*I*) of a Rayleigh atmosphere

247   over a non-Lambertian surface for each specific FOV and Sun-satellite geometry within the

248   Lambertian framework, i.e.,

249         $I = I_0 + GLER \times T/(1 - GLER \times S_b),$ (3)

250   where I_0 is the TOA radiance calculated for a black surface, T is the total (direct + diffuse) solar

251   irradiance reaching the surface converted to the ideal Lambertian-reflected radiance (by dividing

252   by π steradians) and then multiplied by the transmittance of the reflected radiation between the

253 surface and TOA in the direction of a satellite instrument, and S_b is the diffuse flux reflectivity of

254 the atmosphere for the case of its isotropic illumination from below (Dave, 1978). The value of I_0,

255 T, and S_b are pre-computed with VLIDORT and stored in a look-up table. The GLER values are

256 calculated at wavelengths relevant for both NO_2 (440 nm) and cloud (466 nm) retrievals.

257 Over land, the BRDF is calculated using the Ross-Thick Li-Sparse kernel model (Lucht et al.,

258 2000) in VLIDORT (Spurr, 2006):

259 $$BRDF = a_{iso} + a_{vol}k_{vol} + a_{geo}k_{vol}, \tag{4}$$

260 where the coefficients, a_{iso}, a_{vol}, and a_{geo} come from the Moderate Resolution Imaging

261 Spectroradiometer (MODIS) Collection 5 gap-filled, seasonal snow-free BRDF product

262 MCD43GF (Schaaf et al., 2002, 2011) for band 3 (459-479 nm) available at 30 arc-second spatial

263 resolution and 8-day temporal resolution. The term a_{iso} is the isotropic contribution describing the

264 Lambertian part of light reflection from the surface, the volumetric kernel (k_{vol}) describes light

265 reflection from a dense leaf canopy, and the geometric kernel (k_{geo}) describes light reflection from

266 a sparse ensemble of surface objects casting shadows on the background assumed to be

267 Lambertian. The kernels are the only angle-dependent functions, the expressions of which are

268 given in Lucht et al. (2000). The band 3 BRDF coefficients spatially averaged over an actual

269 satellite FOV are used to calculate TOA radiance and GLER at 466 nm. To calculate GLER at 440

270 nm, we apply a scaling method using the ratio of OMI-derived lambert equivalent reflectivity

271 (LER) data at 440 nm and 466 nm:

272 $$GLER_{440} = GLER_{466} \times f_s. \tag{5}$$

273 The value of $f_s = \frac{LER_{440}}{LER_{466}}$ is taken from the gridded monthly LER ratio data at $1° \times 1°$ or coarser

274 resolution. The LER is determined from OMI TOA radiance measurements as discussed in

275 Vasilkov et al. (2017, 2018). We use clear-sky (effective cloud fraction <0.02) and aerosol free

276 (OMI UV Aerosol Index (Torres et al., 2007) <0.5) OMI LER data to create the monthly gridded

277 data. The cloud and aerosol screening is necessary because the spectral dependence of surface

278 features differ from that of clouds and aerosols.

279 Over water, the surface reflectance is calculated at the two wavelengths, 440 nm and 466 nm, using

280 VLIDORT. To calculate TOA radiance, we include light specularly reflected from a rough water

281 surface as well as diffuse light backscattered by water bulk. We also account for contributions

282 from oceanic foam that can be significant for high wind speeds. Reflection from the water surface

283   is described by the Cox–Munk slope distribution function, which depends on both the wind speed

284   and the wind direction (Cox and Munk, 1954). Polarization at the ocean surface is accounted for

285   by using a full Fresnel reflection matrix as suggested by Mishchenko and Travis (1997).

286   We use wind speed data from a pair of satellite microwave imagers that include the Advanced

287   Microwave Scanning Radiometer - Earth Observing System (AMSR-E) instrument onboard the

288   NASA Aqua satellite (Wentz and Meissner, 2004) for 2004-2011 and the Special Microwave

289   Imager/Sounder (SSMIS) onboard the Air Force Defense Meteorological Satellite Program

290   (DMSP) Satellite F16 (Wentz et al., 2012) afterwards. Wind direction data are taken from the

291   Global Modeling Assimilation Office (GMAO) Goddard Earth Observing System Model Forward

292   Processing for Instrument Teams (GEOS-5 FP-IT) near real time assimilation.

293   Diffuse light from the ocean is described by a Case 1 water model with a single input parameter

294   of chlorophyll concentration (Morel, 1988) taken from the monthly Aqua/MODIS data. The

295   common Case 1 water model developed for the Vis (Morel, 1988) was extended to the UV using

296   data from Vasilkov et al. (2002, 2005). To calculate water-leaving radiance, we require the

297   downwelling irradiance at the surface (i.e., atmospheric transmittance). Since the transmittance

298   and the water-leaving contribution are coupled, we develop a simple coupling scheme in

299   VLIDORT that ensures the value of water-leaving radiance used as an input at the ocean surface

300   will correspond to the correct value of the downwelling flux reaching the surface interface

301   (Fasnacht et al., 2019).

302   For OMI ground pixels covering land and water surfaces, the TOA radiance (I) is calculated as an

303   average of radiance for land (I_L) and water (I_w) weighted by the pixel land fraction (f):

304    $$I = fI_L + (1 - f)I_w. \qquad (6)$$

305   The value of f is determined by converting various surface categories in the MODIS data (note

306   that these are of much higher spatial resolution than the OMI data) into a binary land-water mask

307   (e.g., treating all shorelines and ephemeral water as the land category and classifying all other

308   water sub-categories simply as water). The areal fraction of land (or water) for each OMI pixel is

309   then computed as the statistics of the binary categories.

310   Figure 2 shows an example of changes in surface reflectivity used in the previous (V3.1) and the

311   current (V4.0) version of the OMI NO$_2$ algorithm. The GLER data computed for OMI observations

312   as discussed above for March 20, 2005 differ considerably from the OMI-derived climatological

313 monthly LER data (Kleipool et al., 2008) for March. As shown in Figures 2 and 3(a), the GLERs
314 are generally lower than climatological LERs data except at swath edges with large viewing angles
315 and over areas affected by sunglint that correspond to higher values of GLER. Changes over the
316 sunglint areas are rather large, reaching up to 0.3. The climatological LER data derived by
317 analyzing histograms of five years of OMI-based LER data likely overestimate the actual surface
318 reflectivity due to residual cloud and aerosol contamination and underestimate over sunglint areas
319 as the procedure ignores sun glint affected observations. In contrast, the GLER data over land are
320 based on atmospherically corrected radiances from high-resolution MODIS observations,
321 minimizing the impact of both cloud and aerosols.

322 **2.2.2 Improved cloud products retrieval**

323 We develop a new algorithm that provides cloud parameters, namely cloud radiance fraction
324 (CRF) and cloud optical centroid pressure (OCP), and use them in the OMNO2 algorithm. Similar
325 to the standard OMCLDO2 algorithm (Veefkind et al, 2016), our cloud algorithm exploits the O_2-
326 O_2 absorption to retrieve O_2-O_2 SCD as discussed in Section 2.1.2, but derives the two cloud
327 parameters using the GLER and other ancillary data that are used in the NO_2 algorithm,
328 maintaining inter-algorithm consistency. The OMCLDO2 algorithm retrieves these parameters
329 using the climatological LER data from Kleipool et al. (2008). In the following, our new cloud
330 product is referred to as OMCDO2N.
331 The derivation of CRF and OCP is based on a simple cloud model called the mixed Lambertian-
332 equivalent reflectivity (MLER) model (Joiner and Vasilkov, 2006; Veefkind et al., 2016). The
333 MLER model treats cloud and ground as horizontally homogeneous, opaque Lambertian surfaces
334 and mixes them using the independent pixel approximation (IPA). According to the IPA, the
335 measured TOA radiance, I_m, is a sum of the clear-sky (I_g) and overcast (I_c) subpixel TOA
336 radiances that are weighted with an effective cloud fraction (ECF), f_c (e.g., Stammes et al., 2008):

337 $$I_m = I_g(1 - f_c) + I_c f_c. \tag{7}$$

338 We choose the wavelength of 466 nm that is not substantially affected by rotational Raman
339 scattering (RRS) or atmospheric absorption to derive f_c. The parameters I_g and I_c are a function
340 of the ground and cloud LERs, respectively, and are calculated using VLIDORT (Spurr, 2006) and
341 obtained with an interpolated look up table. We use GLER discussed above for ground reflectivity

342 and a uniform cloud reflectivity of 0.8 (Koelemeijer et al., 2001; Stammes et al., 2008). The value

343 of f_c is calculated by inverting Equation (7). Note that aerosols are implicitly accounted for in the

344 determination of f_c, as they are treated (like clouds) as particulate scatters. CRF (f_r) defines the

345 fraction of TOA radiance reflected by cloud:

346 $$f_r = f_c \times \frac{I_c}{I_m}. \qquad (8)$$

347 We use pre-computed look-up tables of the TOA radiances generated using VLIDORT. Due to its

348 wavelength dependence, we calculate CRF at 466 nm for OCP at 440 nm for NO_2 retrievals.

349 The MLER model compensates for photon transport within a cloud by placing the Lambertian

350 surface somewhere in the middle of the cloud instead of at the top (Vasilkov et al., 2008). The

351 pressure of this surface corresponds to OCP, which can be modeled as a reflectance-averaged

352 pressure level reached by backscattered photons (Joiner et al., 2012). We retrieve cloud OCP from

353 the O_2-O_2 SCD discussed above (Section 2.1.2). The cloud OCP, P_c, is estimated by inversion

354 using the MLER method to compute the appropriate O_2-O_2 AMFs:

355 $$SCD = AMF_g \times VCD_g \times (1 - f_r) + AMF_c \times VCD_c \times f_r, \qquad (9)$$

356 where VCD (= SCD/AMF) is the vertical column density of O_2-O_2 over ground (VCD_g) and cloud

357 (VCD_c). The clear-sky (AMF_g) and overcast or cloudy (AMF_c) subpixel AMFs are calculated at

358 477 nm with ground (GLER) and cloud (0.8) reflectivity, respectively. Look-up tables for the

359 AMFs were generated using VLIDORT. Temperature profiles needed for estimation of VCD and

360 AMF are taken from the GEOS-5 global data assimilation system (Rienecker et al., 2011).

361 In addition to OCP, we retrieve the so-called scene pressure. The scene pressure is derived from

362 Eq. (9) assuming that $f_r = 1$ and cloud reflectivity = scene LER. The scene LER is determined

363 from the measured TOA radiance using the equation (Eq. 3) that defines TOA radiance in the

364 Rayleigh atmosphere over a Lambertian surface. In the absence of clouds, aerosols, and any major

365 gas absorptions, the scene pressure should be equal to the surface pressure. The scene pressure is

366 therefore an important diagnostic tool for evaluation of the performance of cloud pressure

367 algorithms.

368   Figure 4 shows an example of cloud products retrieved with our algorithm compared with those
369   retrieved from the standard OMCLDO2 algorithm (Veefkind et al., 2016). The retrieved OCP and
370   CRF from the two algorithms exhibit broadly consistent spatial patterns in both cloud altitude and
371   amount. The values of OCP generally range from 370 hPa to 1001 hPa in OMCDO2N versus 150
372   hPa to 1011 hPa in OMCLDO2N. For both products, CRF varies from 0 for clear-sky to 1 for
373   overcast conditions. A systematic difference is evident with generally higher values in OMCDO2N
374   for OCP by 147 hPa and CRF by 0.01 as compared to OMCLDO2. For OCP, there is a general
375   pattern in difference with OMCDO2N OCP higher for low-altitude clouds (>700 hPa) and lower
376   values for high-altitude clouds (<300 hPa) (Figure 3(c)). The largest OCP differences occur for
377   cases where cloud pressures in OMCLDO2 are clipped to 150 hPa. For CRF, larger differences
378   occur for partially cloudy scenes with higher CRF values in OMCDO2N by 0-0.1 for both land
379   and water surfaces (Figure 3(b)). Exceptions are over sun-glint areas, where CRF in OMCDO2N
380   is lower by 0-0.3 with the mean difference of 0.13.

381   **2.2.3 Treatment over snow and ice surfaces**

382   Over ice and snow surfaces, identified by the Near-real-time Ice and Snow Extent (NISE) flags
383   (Nolin et al., 2005) in the OMI Level 1b data, the following treatments are made for surface
384   reflectivity. In case of permanent ice and snow surfaces, the MCD43GF product provides BRDF
385   parameters, allowing us to calculate GLER. Over seasonal snow area usually with data gaps in
386   MCD43GF, we calculate OMI-derived LER but capped by a constant snow albedo of 0.6 following
387   Boersma et al. (2011). In rare cases of pixels not flagged by NISE and gaps in MODIS data, we
388   use OMI LER climatology (Kleipool et al., 2008), regardless whether the surface is either snow/ice
389   covered but missed by NISE or snow/ice free.

390   The OMI-derived scene reflectivity and scene pressure are used for NO_2 and cloud retrievals over
391   seasonal snow covered areas. If the NISE flags are set as true, the following assumptions are made
392   in our CRF, OCP, and NO_2 retrievals. Over bright surfaces (scene reflectivity > 0.2), we consider
393   the scenes as snow or cloud covered and assign the scene pressure to OCP. In addition, if a
394   difference between the surface pressure and scene pressure is smaller than 100 hPa, the scene is
395   considered to be either cloud free or covered by optically thin clouds following the cloud over
396   snow classification by Vasilkov et al. (2010), and CRF for the pixel is set to zero. If the difference
397   between the surface pressure and scene pressure exceeds 100 hPa, the scene is considered to be
398   overcast by optically thick (shielding) clouds (Vasilkov et al., 2010), and CRF for the pixel is set

399 to one. To avoid a possible NISE misclassification (Cooper et al., 2018) for low-reflectivity scenes

400 (scene reflectivity < 0.2), we consider such scenes as being snow/ice-free and calculate CRF, OCP,

401 and NO_2 AMF using the standard procedure with GLER for those scenes.

2.2.4 Improved terrain height/pressure calculation

403 Terrain pressure is a critical parameter to the AMF in NO_2 and cloud algorithms as well as to the

404 total optical depth of the Rayleigh atmosphere in the GLER algorithm. Prior studies have shown

405 that errors in terrain pressure can introduce over 20% errors in retrieved NO_2 VCD, especially in

406 areas of complex terrain (Zhou et al, 2010; Russell et al., 2011).

407 Here, we use a 2-arc minute Global Relief Model of global land-water surface data (ETOPOv2,

408 National Geophysical Data Center, 2006) to derive terrain height for each individual OMI ground

409 pixel. We derive the pixel-average terrain height by collocating and averaging the high resolution

410 data as discussed in Qin et al. (2019). The corresponding terrain pressure for each OMI pixel (P_s)

411 is calculated from the terrain pressure-height relationship established based on MERRA-2 monthly

412 terrain pressure (P_{s_GMI}) at a spatial resolution of 1° latitude × 1.25° longitude used in the GMI

413 model discussed above:

$$P_s = P_{s\_GMI} e^{-\left(\frac{\Delta z}{H}\right)}, \tag{10}$$

415 where Δz ($= z - z_{GMI}$) represents the difference between the average terrain height for an OMI

416 pixel (z) and the terrain height at GMI resolution (z_{GMI}). The parameter, $H = \frac{kT}{Mg}$, represents the

417 scale height, where k is the Boltzmann constant, T is the temperature at the surface, M is the mean

418 molecular weight of air, and g is the acceleration due to gravity.

2.3 Impact of the changes on AMF

420 Figure 5 shows an example of how changes in each individual input parameter affect tropospheric

421 AMFs which, in turn, translate inversely to tropospheric NO_2 column retrievals. Replacing

422 climatological LER from OMLER with daily GLER data affects scattering weight profiles in the

423 lower troposphere, resulting in lower values of tropospheric AMF almost everywhere, except over

424 sun glint areas, where the use of GLER enhances scattering weights and tropospheric AMF (Figure

425 5(a)). The changes in tropospheric AMF with GLER usually range from -50% to 25%,

426 occasionally reaching up to -100%. The effect is small (-6% to 1%) for overcast scenes (CRF>0.9),

427   and increases (-28% to 17%) over clear and partially cloudy scenes (CRF<0.5), for unpolluted

428   regions, and surges (-62% to 3%) over polluted areas ($>5\times10^{15}$ molec. cm^{-2}). Figure 6(a) shows

429   GLER-driven changes in clear-sky (CRF<0.5) tropospheric AMF for different surface and scene

430   types, separated by tropospheric NO$_2$ column amounts. For 80% of cases over land, 97% over

431   water outside of sunglint areas, and 98% over sunglint areas, tropospheric NO$_2$ columns are <

432   1.5×10^{15} molec. cm^{-2} and the average GLER-driven differences are small at –6.6±17.3%, -

433   3.8±7.1%, and 4.0±12.9%, respectively. The differences increase gradually with column amount

434   over NO$_x$ source regions (e.g., cities and highly polluted coastal areas) with binned (of size 1×10^{15}

435   molec. cm^{-2}) average differences ranging from -10±20.1% to -30±19.7%. Over snow and ice

436   surfaces, changes are rather large, reaching up to a factor of two. The impact of change in the

437   surface reflection data on stratospheric AMFs is negligible (<2%).

438   Figures 5(b) and 6(b) show how changes in the cloud parameters (CRF and OCP) affect

439   tropospheric AMF. Replacing OMCLDO2-based cloud parameters with those from OMCDO2N

440   changes scattering weight profiles in a complicated way. Higher values of OCP in OMCDO2N

441   will include additional portions of scattering weights between the OMCDO2N- and OMCLDO2-

442   based OCPs, especially in the lower troposphere, thereby reducing the tropospheric AMF. On the

443   other hand, the higher CRF values lead to an increased contribution of the cloudy AMF in the

444   calculation of tropospheric AMF, thereby increasing its value. Their combination causes a wide

445   range of scenarios as well as large variation in the AMF effect. Overall, the change in cloud

446   parameters causes enhancement of tropospheric AMFs for partially cloudy and overcast scenes

447   and reduction for clear-sky scenes, especially over polluted areas. The AMF differences are

448   generally large for low AMF values that are driven by enhanced differences in either OCP, CRF,

449   or both as discussed in Vasilkov et al (2017). The changes in tropospheric AMF with the

450   OMCDO2N-based cloud parameters usually range from -17% to 28% with a larger variation over

451   land (-34% to 40%) as compared to water (-12% to 25%), and for low (<1) AMF (-47% to 41%)

452   as compared to high (>3) AMF (-4% to 18%). The largest changes in AMF (-96% to 62%) occur

453   over snow and ice surfaces that result from the difference in the treatment of snow and ice for

454   cloud and NO$_2$ retrievals as discussed in Section 2.2.3. For clear-sky and partially cloudy scenes

455   with CRF < 0.5, the effect of the changes in cloud parameters differs between land and water

456   surfaces as well as sunglint and non-sunglint geometries and becomes more pronounced over

457 polluted land and coastal areas (Figure 6b). As in the case of surface reflectivity, the impact of the

458 change in cloud parameters on stratospheric AMF is <1%.

459 Figure 5c presents an example of changes in tropospheric AMF differences between the previous

460 approach of using terrain pressure at OMI pixel centers and the pixel average terrain pressure

461 implemented in the current version (V4.0). In general, the AMF changes driven by the changes in

462 terrain pressure are within ±1% over ocean and ±3% over land, although at times they can reach

463 up to 30%, especially for observations over complex terrain such as mountainous regions (Figure

464 5c inset).

465 Figures 5d and 6c show the AMF differences arising from the combined effect of changes in all

466 parameters discussed above. The effect arising from the replacement of the climatological OMLER

467 with GLER is partially compensated by the effect arising from the change in cloud parameters in

468 places where the two parameters exhibit opposite trend. Exceptions are over polluted land and

469 coastal areas, the GLER effect on AMF is augmented by the cloud effect. The average AMF

470 changes arising from all parameters (2%) are lower than the changes arising from either GLER (-

471 2.3%) or cloud parameters (4.1%), although the combined effect leads to a wider range of variation

472 in AMF changes (-100% to 57%) as compared to the effect from individual parameters. The

473 changes arising from all parameters are somewhat smaller (-21% to 34%) for overcast scenes

474 (CRF>0.9) as compared to (-47% to 29%) over clear and partially cloudy scenes (CRF<0.5), and

475 are substantial (-137% to 30%) over highly polluted areas ($>5\times10^{15}$ molec. cm^{-2}) and over snow/ice

476 surfaces (-126% to 99%). Differences in the AMF effect are evident among land, water, and

477 sunglint areas (Figure 6c). The impact of the changes is below 1% for the stratospheric AMF.

478 **2.4 Row anomaly and removal of stripes**

479 The retrieved NO$_2$ SCDs have persistent relative biases in the 60 cross-track FOVs and show a

480 pattern of stripes running along each orbital track. This instrumental artifact is corrected using the

481 "de-striping" procedure described in detail in Bucsela et al (2013). Briefly, the de-striping

482 algorithm estimates the mean cross-track biases using measurements obtained at latitudes between

483 30S and 5N and from orbits within 2 orbits of target orbit. These correction values, one for each

484 cross-track position, are then subtracted from the retrieved SCDs to derive the de-striped SCD

485 field.

486 Starting June 25, 2007 and presumably even earlier, OMI experienced a more severe form of
487 anomaly that affects the quality of radiance data in certain rows at all wavelengths (Dobber et al.,
488 2008; Schenkeveld et al., 2017). This effect, called the "row anomaly" (RA), has developed and
489 changed over time. Currently, the RA has affected approximately half of the OMI's FOVs,
490 resulting in OMI's global coverage now in two days instead of one before the onset of the RA.
491 The quality of radiance data for the RA-affected FOVs is sufficiently poor as to prevent reliable
492 NO$_2$ retrievals. Therefore, we abandon retrieval calculations for all measurements that are flagged
493 by the RA-detection algorithm used in the Level-1 processing. We found that this RA-detection
494 algorithm may not be sufficiently sensitive to the relatively small (but important for our purposes)
495 RA changes. Figure 7 shows an example of anomalous rows not flagged by the RA-detection
496 algorithm but observed in the NO$_2$ retrievals. Shown are time series of average NO$_2$ SCDs
497 normalized by geometric AMFs over the Pacific Ocean for the RA-unaffected row of 20 (0-based)
498 compared with three rows that show significant degradation in the quality of SCD retrievals. These
499 particular rows are in the immediate proximity to the main RA area, thus showing the gradual RA
500 evolution: at the present epoch the RA slowly shifts towards the high-numbered rows – note the
501 sequential timing of the big drops in the retrievals in the rows 44-46. While the data from the three
502 rows start deviating from row 20 beginning from summer 2016, the data quality degrades further
503 for rows 44, 45, and 46 from September of 2017, 2018, and 2019, respectively, to the extent that
504 they cannot be sufficiently corrected by the de-striping algorithm. In such cases, we implement
505 additional RA-flagging for those rows that start showing anomalous behavior, and exclude those
506 data from Level-2 and higher level NO$_2$ products.

507 **2.5 Calculation of stratospheric and tropospheric NO$_2$ columns**

508 We use an observation-based stratosphere-troposphere separation scheme to estimate the
509 stratospheric NO$_2$ field as discussed in detail in Bucsela et al. (2013), and the algorithm remains
510 unchanged in the current version. Briefly, the stratospheric field for an orbit is computed by
511 creating a gridded global field of initial stratospheric NO$_2$ VCD estimates (V_{init}) with data
512 assembled from within ±7 orbits of the target orbit:

513    $$V_{init} = \frac{S_{strat}}{AMF_{strat}} = \frac{S - S_{trop\_ap}}{AMF_{strat}}. \qquad\qquad (11)$$

514 Here S_{strat} and AMF_{strat} represent stratospheric SCD and AMF, respectively. An a priori
515 estimates of the tropospheric contribution (S_{trop_ap}) are subtracted from the measured, de-striped

516 SCDs (S), and grid cells where this contribution exceeds 0.3×10^{15} molecules cm^{-2} are masked.
517 This masking ensures that the model contribution to the retrieval is minimal, especially in the
518 polluted areas. The residual field of the initial stratospheric VCDs measured outside the masked
519 regions mainly over unpolluted or cloudy areas is smoothed by a boxcar average and a 2-
520 dimensional interpolation, yielding an estimate for stratospheric NO$_2$ VCD (V_{strat}) for an
521 individual ground pixel.

522 The estimation of the stratospheric NO$_2$ VCD allows for the computation of the tropospheric NO$_2$
523 VCD (V_{trop}) from the de-striped NO$_2$ SCD (S) and the tropospheric AMF (AMF_{trop}):

524 $$V_{trop} = \frac{S_{trop}}{AMF_{trop}} = \frac{S - S_{strat}}{AMF_{trop}}, \qquad\qquad (12)$$

525 where stratospheric NO$_2$ SCD (S_{strat}) is calculated from stratospheric AMF (AMF_{strat}) and V_{strat}
526 computed in the previous step.

527 With the updates in surface and cloud treatments as discussed in Section 2.2, the current version
528 has made significant improvements particularly in tropospheric AMFs and consequently in VCD
529 estimates. Further improvement to the retrievals is possible by enhancing the quality of a priori
530 NO$_2$ profiles through improvements in model resolution, emissions, and chemistry, which remain
531 unchanged in the current version. If improved a priori NO$_2$ profiles become available, one can first
532 use Eq. 1 to readily re-calculate AMF_{trop} by combining them with scattering weights ($w_{(z)}$)
533 archived in the data files and then use Eq. 12 together with other supplied parameters to re-
534 calculate V_{trop}. The same approach can be applied to remove the effect of a priori profiles used in
535 retrievals altogether, while comparing NO$_2$ columns from a model simulation with retrievals
536 (Eskes and Boersma, 2003; Lamsal et al., 2014).

537 Figure 8 shows a comparison of tropospheric and stratospheric NO$_2$ columns retrieved from V3.1
538 and V4.0 algorithms for 20 March, 2005. As expected, the updates implemented in V4.0 yield
539 higher (~10–40%) tropospheric NO$_2$ columns in polluted areas, with less-pronounced (±10%)
540 differences in background and low-column areas. These results are consistent with the observed
541 differences in the tropospheric AMF as discussed above in Section 2.2.4 as well as with other
542 previous regional studies over land surfaces (Zhou et al, 2010; McLinden et al, 2014; Lin et al.,
543 2014, 2015; Laughner et al., 2019; Liu et al., 2019) that implemented one or more of the changes
544 applied in V4.0. In contrast to changes in tropospheric NO$_2$ retrievals, changes in stratospheric
545 NO$_2$ estimates range between -3.6×10^{14} molec. cm^{-2} and 3.2×10^{14} molec. cm^{-2} and are close to the

546 range of expected uncertainties of stratospheric NO_2 estimates (Bucsela et al., 2013). The relative
547 differences in stratospheric NO_2 column between the two versions is close to 0% on average,
548 usually range between -2.5% and 2.0%, and occasionally reach up to ±13%. This difference in
549 stratospheric NO_2 estimates is much larger than the difference in stratospheric AMFs and is caused
550 by differences in tropospheric AMFs that influence NO_2 observations over unpolluted and cloudy
551 areas used by the stratosphere-troposphere separation scheme.
552 Figure 9 shows the seasonally averaged tropospheric NO_2 columns over the selected domains of
553 North America, Europe, southern Africa, and Asia for the months of June, July, and August in
554 2005. These domains contain highly polluted areas with significant NO_x emissions where the
555 impact of changes in surface reflectivity and cloud parameters on tropospheric NO_2 retrievals
556 becomes increasingly important. The use of more accurate pixel-specific information for surface
557 and cloud parameters in V4.0 results in significantly enhanced tropospheric NO_2 column retrievals
558 almost everywhere. The effect, however, varies with the vertical distribution of NO_2, with the
559 largest effects in high-column areas. This spatially-varying effect arising from algorithm changes
560 could have significant implications for estimates of trends and emissions of NO_x from satellite
561 observations.
562 Figure 10 shows the seasonal average tropospheric NO_2 columns for December through February.
563 While seasonal differences in NO_2 columns are evident owing to changes in NO_x lifetime and
564 boundary layer depth, the impact of algorithm changes in V4.0 remains similar. There are two
565 notable exceptions specifically related to observations over snow and ice surfaces. First, there are
566 significant data gaps in V3.1 but nearly none in V4.0. In V3.1, retrievals over snow and ice areas
567 were considered to be highly uncertain and therefore discarded, following the recommendation of
568 Boersma et al. (2011). As discussed above in Section 2.2.3, V4.0 incorporates changes in surface
569 and cloud treatment in NO_2 algorithm that allows us to retain more observations that we determine
570 to be our acceptable level of cloudiness. Next, these algorithm changes led to profound changes in
571 the calculated tropospheric AMFs and resulting NO_2 column amounts. The reduction in
572 tropospheric NO_2 retrievals in V4.0 over snow and ice covered surfaces arises from a combined
573 effect of enhanced values of surface reflectivity, their impact on the CRF and OCP retrievals, and
574 an inconsistent number of samples used in the calculation of the seasonal average. Nevertheless,
575 due to inferiority in the quality of BRDF data as well as complexities in separating snow from
576 clouds, caution is needed when interpreting winter time data at high latitudes.

577 Figure 11 shows some examples of how changes in the algorithm from V3.1 to V4.0 affect monthly
578 domain average tropospheric NO_2 columns over areas affected by various NO_x sources. In contrast
579 to minor changes over the pristine Pacific Ocean, month-to-month changes over source regions
580 vary considerably. The differences in tropospheric NO_2 columns between V4.0 and V3.1 range
581 from -11 to 15% over Beijing, China and from 0 to 29% over the Ruhr area in Germany, suggesting
582 variations in relative differences among cities and industrial areas. The changes over a major
583 biomass burning area of Democratic Republic of Congo, Angola, and Zambia range 13-56%
584 during the biomass burning season of May through August, but are <5% in other months.
585 Differences between the two versions are small over areas influenced by lightning NO_x emissions.
586
587 In Figure 12, we examine monthly variation of tropospheric NO_2 columns from the two versions
588 over five highly populated and polluted cities that vary in terrain types ranging from coastal (e.g.,
589 Shanghai, Tokyo) to mountainous (e.g., Mexico City). NO_2 columns in V4.0 are generally higher
590 than V3.1 by 0-30%, but the difference can occasionally reach up to 50% in some months. Changes
591 of that order of magnitude in highly polluted areas have implications for estimation of NO_x
592 emissions and trends using these data.

593 **3 Assessment of OMI NO_2 product**

594 In this section, we compare OMI NO_2 columns with total column retrievals from ground-based
595 Pandora measurements and integrated tropospheric columns from aircraft spirals at several
596 locations of the DISCOVER-AQ (Deriving Information on Surface Conditions from COlumn
597 and VERtically Resolved Observations Relevant to Air Quality) field campaign held between
598 2011 and 2014.

599 **3.1 Comparison between OMI and Pandora total column NO_2**

600 Here, we compare the total column NO_2 retrievals from OMI and the ground-based Pandora
601 spectrometer. Pandora is a compact sun-viewing remote sensing instrument that provides estimates
602 of NO_2 column amounts from the surface to the top of the atmosphere (Herman et al., 2009, 2018).
603 The NO_2 retrieval approach for Pandora is similar to that of OMI and consists of the DOAS spectral
604 fitting procedure to derive NO_2 SCD and its conversion to VCD using AMFs. However, the details

605 differ due to the lack of top-of-atmosphere radiance measurements for the spectral fitting and
606 simplicity in the AMF calculation for Pandora due to its direct sun measurements.

607 To compare with the OMI observations, we use Pandora data for sites listed in the Pandonia Global
608 Network (https://www.pandonia-global-network.org/). Out of 22 sites, we select 18 sites that we
609 determined to be suitable for comparison. Data from some of the sites (e.g., Rome, Italy) are
610 consistently higher than OMI by over a factor of two, suggesting that the sites may be in close
611 proximity to local sources that cannot be resolved by OMI. Although, some of the selected sites
612 have sporadic and short-term measurements (e.g., Ulsan, S. Korea), we consider them for
613 improved sampling and coverage. The collocation criteria include spatial and temporal matching
614 between OMI and Pandora observations by selecting the OMI pixels that encompass the Pandora
615 site and using Pandora 80-sec total NO_2 column data averaged over ±10 minutes of OMI
616 observations. We use high quality data obtained under clear sky conditions with root-mean-square
617 of spectral fitting residuals < 0.05 and NO_2 retrieval uncertainty < 0.05 DU (~1.3×10^{15} molec. cm$^-$
618 ^{2}) for Pandora and with CRF < 0.5 for OMI.

619 Figure 13 shows a comparison of OMI total NO_2 columns (sum of tropospheric and stratospheric
620 columns) with coincidently sampled Pandora direct-sun NO_2 column retrievals at a clean site of
621 Izaña in Tenerife Island, Spain, and a more polluted site in Greenbelt (Maryland, USA). The Izaña
622 Atmospheric Observatory is located on the top of a mountain plateau, with an elevation of 2373
623 meters above sea level. Since the site is free of local anthropogenic influences, Pandora
624 observations likely provide stratospheric and free tropospheric NO_2 amounts. In contrast, the
625 Greenbelt site in a suburban Washington DC area has traffic and air quality typical of polluted US
626 cities. As shown in Figures 13(a) and 13(b), OMI NO_2 retrievals from the two versions are highly
627 consistent (r>0.92) with somewhat higher values in V4.0 as compared to V3.1, by on average 13%
628 in Greenbelt and just 1% in Izaña. The variations of OMI NO_2 from both versions are also broadly
629 consistent with the Pandora measurements. The OMI and Pandora NO_2 columns are fairly
630 correlated (r = 0.32, N = 232) at Izaña, and moderately correlated (r = 0.51, N = 123) at Greenbelt;
631 often times the differences between each individual OMI and Pandora observations are significant.
632 Overall, the total column NO_2 data from OMI is higher than Pandora, with the average difference
633 of <16%. Occasional large discrepancies between OMI and Pandora reflect a combination of

634 spatial heterogeneity, differences in spatial and temporal sampling, differences in vertical

635 sensitivity of satellite and ground-based observations, and errors in OMI and Pandora retrievals.

636 Figures 13(c) and 13(d) show the multi-year monthly mean variation of OMI and Pandora NO_2

637 columns. The seasonal variation in Pandora and OMI NO_2 columns is highly consistent and

638 exhibits a summer maximum and a fall minimum at Izaña, and a winter maximum and summer

639 minimum in Greenbelt. The seasonal variation in the total column reflects that of the stratosphere

640 for Izaña and of the troposphere in Greenbelt. For Izaña, the monthly mean differences between

641 OMI and Pandora range from 8.2% in June to 38% in October for V4.0 and from 7.0% in June to

642 37% in October for V3.1. This discrepancy is likely due to the large aerial coverage of OMI pixels

643 including nearby cities, unlike the point measurements made by Pandora at the mountain top. The

644 average tropospheric NO_2 column observed by OMI is 8.9×10^{14} molec cm^{-2}, suggesting significant

645 NO_2 amounts in the troposphere with 20-32% contributions to total column NO_2 on a monthly

646 scale. For Greenbelt, the monthly mean differences between OMI and Pandora are within $\pm 12\%$

647 for the majority of the cases for both versions, with V4.0 improving agreement for February, April,

648 May and December, and worsening somewhat in other months, especially in September and

649 November, when the two versions exhibit larger differences in tropospheric NO_2 retrievals.

650 Figure 14 shows average total NO_2 columns measured by Pandora and OMI at the 18 selected

651 sites. Although there is a wide range of differences between individual sites, Pandora and OMI

652 observations exhibit a good spatial correlation, with slightly improved correlation for V4.0

653 (r=0.65, N=1082) as compared to V3.1 (r=0.62). The site-specific average values generally agree

654 to $\pm 35\%$ for columns $< 10^{16}$ molec. cm^{-2}. For more polluted sites, OMI retrievals tend to be lower

655 than the Pandora data. Although the relationship between Pandora and OMI has not changed

656 appreciably with the updates made in the OMI V4.0 product, the corrections are in the right

657 direction for a majority of the sites. The observed differences should not be interpreted as biases

658 in retrievals but rather as the combined effect of differences in spatial coverage, heterogeneity in

659 the NO_2 field, preferential placement of Pandora instruments, and potentially, a lack of site-

660 specific profile shapes assumed in OMI retrievals.

661 **3.2 Assessment using DISCOVER-AQ observations**

662 We also use NO_2 observations from the DISCOVER-AQ field program to assess OMI NO_2

663 retrievals. The DISCOVER-AQ campaign was composed of four field deployments: Baltimore-

664 Washington area in Maryland (MD) in July 2011; the San Joaquin Valley in California (CA) in

666 January-February 2013; Houston, Texas (TX) in September 2013; and Denver, Colorado (CO) in

667 July-August 2014. An observing strategy of the campaign was to carry out systematic and

668 concurrent in situ and remote sensing observations from a network of ground sites and research

669 aircraft that spiraled over each site 2-4 times a day. The payload of the P-3B research aircraft

670 included in situ measuring instruments to measure NO_2 profiles in the 0.3-5 km altitude range.

671 Each campaign hosted ground-based networks of surface monitors to provide in situ NO_2

672 observations as well as Pandora spectrometers to measure NO_2 column amounts.

673 We use Pandora NO_2 column observations and in situ NO_2 spiral data spatially and temporally

674 matched to OMI on clear and partially cloudy (cloud radiance fraction < 0.5) days. Airborne

675 measurements were carried out using the 4-channel chemiluminescence instrument from the

676 National Center for Atmospheric Research (Ridley and Grahek, 1990) and the Thermal

677 Dissociation Laser-Induced Florescence from the University of Berkeley (Thornton et al., 2000).

678 Despite differences in the measurement technique and sampling strategy, NO_2 measurements from

679 the two instruments are highly consistent and generally agree within 10%, with the exception of

680 ~32% difference for Houston (Choi et al., 2020). Here, we use the 1-second merged data from the

681 chemiluminescence instrument only, taking advantage of its high frequency measurements. The

682 spiral data are extended to the ground by using coincident in situ surface NO_2 measurements

683 sampled over the duration of spiral (~20 minutes). To account for NO_2 amounts in the missing

684 portion from the highest aircraft altitude to the tropopause, we use NO_2 from the GMI simulation.

685 Like the surface data, the Pandora total column NO_2 data are averaged over the duration of each

686 aircraft spiral. For OMI, we include data from all cross-track positions that are not subject to the

687 row anomaly.

688 Figure 15 and Table 2 show a summary of the comparison of OMI V4.0 and V3.1 NO_2 columns

689 with vertically integrated tropospheric columns from the P-3B aircraft at 20 spiral locations.

690 Overall, tropospheric NO_2 columns from OMI and aircraft spirals suggest a poor agreement but a

691 good correlation (r=0.74, N=100), with slightly improved agreement for V4.0 as compared to

692 V3.1. The agreement and correlations between OMI and P-3B observations vary by campaign

693 locations (e.g., r=0.4 for MD to r=0.81 for CA for V4.0). The level of improvements from V3.1 to

694 V4.0 also vary from 1.2% in TX to 9.8% in CA. OMI retrievals are usually lower than the aircraft

695 data, with larger differences for sites with larger NO_2 gradients and columns (e.g., Denver La Casa,

696 CO; Fresno, CA). OMI is rarely higher than the aircraft data as this usually happens over relatively

cleaner sites (e.g., Fairhill, MD). This alternating nature of the variation in results in polluted versus clean areas suggests that OMI's large footprint size and narrow spiral radius (~4 km) of the aircraft are likely the primary cause for the observed differences. This was demonstrated in Choi et al. (2020) by using high-resolution Community Multi-scale Air Quality Model (CMAQ) simulations. Additional contributions to the observed differences could come from OMI retrieval errors arising from the use of a coarse resolution GMI-based a priori NO_2 profile shapes in the AMF calculation. Such profile-related retrieval errors can be partially accounted for by replacing GMI profiles with the aircraft observed NO_2 profiles (OMI_{obs}). The use of observed profiles in the OMI retrievals from both versions leads to a slight change in correlation, but 20-35% reduction in mean difference between OMI and aircraft observations, highlighting the role of a priori profiles in NO_2 retrievals as suggested by previous studies (Russell et al., 2011; Lamsal et al., 2014; Goldberg et al., 2017; Laughner et al., 2019; Choi et al., 2020). The campaign-average difference between OMI and aircraft observations is -38.8% in V3.1 and -23.1% in V4.0, resulting in a net improvement of 15.7% with V4.0. We note here that the aircraft observed profiles can be very different from the actual profiles over OMI's FOVs (pixels) due to a difference in the sampling domains for the two measurements.

Figure 15 and Table 3 also show the comparison between the OMI and Pandora total column retrievals at the 20 DISCOVER-AQ sites. The correlations between collocated OMI V4.0 and Pandora observations for individual campaign locations vary from fair (r=0.13 for MD) to good (r=0.70 for CO), with a moderate correlation (r=0.56, N=83) for all observations from the four locations. The changes in correlation from V3.1 to V4.0 are generally small with a minor improvement in CA and deterioration in MD. As compared to the aircraft observations, the OMI data generally show better agreement with the Pandora retrievals, with the smallest difference in MD and the largest difference in CO. As compared to V3.1, the agreement is improved for V4.0 by up to 9%. The use of aircraft-observed NO_2 profiles in AMF calculations leads to higher OMI column retrievals than those from Pandora for MD and TX, and lower columns than Pandora for CA and CO. Overall, total column retrievals from OMI V3.1 and V4.0 are respectively 33.5% and 16.3% lower than Pandora; this change is consistent with the comparison between OMI and P-3B observations. The observed discrepancy between the OMI, aircraft spiral, and Pandora data points

Deleted: 2

729 to general difficulties in comparing observations of different spatial resolutions for a short-lived

730 trace gas like NO_2 that has large spatial gradients, especially in the boundary layer.

731 **4 Conclusions**

732 We have described a series of significant improvements made to the operational OMI NO_2

733 Standard Product (OMNO2) algorithm. The new version, version 4.0 (V4.0), of the OMNO2

734 product, released recently to the public at the NASA Goddard Earth Sciences Data and Information

735 Services Center (GES DISC), mainly relies on improved methods and high-resolution inputs for a

736 more accurate determination of air mass factors (AMFs). Major improvements include (1) a new

737 O_2-O_2 cloud algorithm to estimate cloud radiance fraction (CRF) and cloud optical centroid

738 pressure (OCP), both required for the AMF calculation; 2) a new MODIS BRDF-derived

739 geometry-dependent surface Lambertian Equivalent Reflectivity (GLER) input data used in both

740 the NO_2 and cloud retrievals; (3) improved terrain pressure calculated for OMI's footprint; and (4)

741 improved surface and cloud treatments over snow and ice surfaces. Over open-water areas, inputs

742 to the GLER calculations include chlorophyll concentrations from MODIS, the wind speed data

743 from the Advanced Microwave Scanning Radiometer–Earth Observing System (AMSR-E) and

744 the Special Microwave Imager–Sounder (SSMIS) instruments, and the wind direction data from

745 the NASA GEOS-5 model. The following algorithmic steps remain unchanged: the scheme for

746 separating stratospheric and tropospheric components, first implemented in Version 2.1 (Bucsela

747 et al., 2013; Lamsal et al., 2014); an optimized spectral fitting algorithm used for NO_2 slant column

748 density retrievals (Marchenko et al., 2015); and the use of annually varying monthly mean Global

749 Modeling Initiative (GMI) derived inputs (e.g., NO_2 vertical profile shapes), as implemented in

750 Version 3.0 (Krotkov et al., 2017).

751 The changes in inputs result in substantial changes tropospheric AMFs (and thus VCDs) in V4.0

752 relative to the previous version (V3.1). The geometry-dependent GLER data computed for OMI

753 observations used in V4.0 differ considerably from the OMI-derived climatological LER data

754 (Kleipool et al., 2008) used in V3.1. The data from GLER (a unitless value with 0.0-1.0 range) are

755 generally lower, by <0.05, than the climatological LER data over land and ocean outside of

756 sunglint areas; GLER is much higher over the sunglint areas that reaches more than 0.3 due to the

757 geometry-dependent Fresnel reflection. The cloud parameters (OCP and CRF) retrieved from the

758 new O_2-O_2 cloud algorithm described here and those from the operational cloud algorithm

760 (Veefkind et al., 2016) used in V3.1 exhibit significant differences with generally larger values for

761 both parameters in V4.0 as compared to V3.1, with noticeable exceptions over sunglint areas,

762 where CRFs in V4.0 are lower than V3.1 by <0.3. Over snow and ice surfaces, identified by the

763 Near-real-time Ice and Snow Extent (NISE) flags in the OMI L1b data, various adjustments are

764 made in V4.0 for GLER, OCP, and CRF by using other diagnostic parameters (e.g., scene pressure)

765 retrieved by the new cloud algorithm. The scattering weights and tropospheric AMFs for NO_2

766 respond to the changes in these input parameters in a complicated way. Typically, tropospheric

767 AMFs decrease with the use of GLER and increase with the use of the new cloud parameters, with

768 exceptions over water surfaces affected by sunglint, where we observe the opposite effect. Over

769 highly polluted areas, the effect from GLER is augmented by the effect from the new cloud

770 parameters, resulting in a considerable decrease in the tropospheric AMF. Changes in tropospheric

771 AMFs resulting from the updates in treatment of the snow and ice-covered areas are also

772 significant. Changes in the adopted terrain pressure (V4.0 vs V3.1) can also have a sizable effect

773 on tropospheric AMFs, particularly over areas with a complex terrain. In contrast, for stratospheric

774 AMFs the combined impact of all of these algorithmic updates is negligible.

775 The changes in tropospheric AMFs translate directly into changes in tropospheric NO_2 retrievals

776 and indirectly into stratospheric NO_2 estimates. Over background and low column NO_2 areas,

777 tropospheric NO_2 column estimates have not changed appreciably from V3.1 to V4.0. Over more

778 polluted areas, the tropospheric NO_2 retrievals have typically increased by 10-40% from V3.1 to

779 V4.0, mostly in a direct proportion to the pollution level. Most of the increase in the highly polluted

780 areas is driven by the change in the surface reflectivity data used in the AMF calculation, with

781 additional increase due to changes in the cloud parameters. Changes in the stratospheric NO_2

782 estimates are usually within ±2.5%, which is close to the range of estimated uncertainties of

783 stratospheric NO_2 estimates.

784 A global assessment of V4.0 tropospheric and stratospheric NO_2 products was performed by a

785 thorough evaluation of their consistency with the data from V3.1, which was carefully evaluated

786 in our previous works (e.g., Krotkov et al., 2017; Choi et al., 2020). In addition, we use

787 NO_2 measurements made by independent ground- and aircraft-based instruments to evaluate the

788 V4.0 product. The comparison of OMI total column NO_2 data with collocated Pandora

789 observations at its 18 global network and 20 DISCOVER-AQ locations suggests that OMI and

790 Pandora are generally highly consistent, exhibit similar seasonal variation, and agree within their

791 expected uncertainties of 2.7×10^{15} molec cm^{-2} for Pandora (Herman et al., 2009) and ~30% for
792 OMI under clear-sky conditions (Boersma et al., 2011; Bucsela et al., 2013). Individual data points
793 differ considerably, and OMI tends to be lower than Pandora over highly polluted areas with
794 spatially inhomogeneous NO$_2$. The comparison of OMI tropospheric NO$_2$ column retrievals with
795 columns derived from the aircraft spirals and surface data during the DISCOVER-AQ campaign
796 also suggests general agreement in spatial variation, but OMI values are about a factor of two
797 lower in polluted environments. This difference is due partly to inaccurate a priori assumptions,
798 but primarily to OMI's relatively large pixels. The use of observed NO$_2$ profiles as a priori
799 information reduces the bias from ~50% to 23%, on average. The Multiple-Axis Differential
800 Optical Absorption Spectrometer (MAX-DOAS) (e.g., Chan et al., 2019) or high spatial resolution
801 measurements from aircraft (e.g., Nowlan et al., 2016; Lamsal et al., 2017; Judd et al., 2019) would
802 provide a more comprehensive validation by mapping the NO$_2$ distributions over the complete
803 areas of aircraft spirals and the satellite FOVs.

804 In this study, we focused on improving the surface and cloud parameters in the NASA standard
805 NO$_2$ product retrievals. To further improve the retrieval accuracy, it is important to incorporate
806 improved retrieval methods and auxiliary information, such as high resolution a priori NO$_2$
807 profiles. For instance, current cloud algorithms based on the MLER model treat aerosols implicitly
808 by providing effective (cloud + aerosol) CRF and effective cloud OCP, both necessary inputs for
809 AMF calculations. Cloud effects on trace gas retrievals can be compromised by the unknown
810 aerosol effects, which lead to errors in AMF calculations. Therefore, the use of the GLER product
811 in the NO$_2$ algorithm will greatly benefit from an explicit accounting for aerosol effects,
812 particularly over polluted regions. We have recently developed an explicit and consistent aerosol
813 correction method which can be applied consistently in both the cloud and NO$_2$ retrievals
814 (Vasilkov et al. 2020); it uses a model of the aerosol optical properties from a global aerosol
815 assimilation system paired with radiative transfer calculations. This approach allows us to account
816 for aerosols within the OMI cloud and NO$_2$ algorithms with relatively small changes and will be
817 used in the next version of the NO$_2$ algorithm.

818

819 **Code/Data availability:** The Level-2 swath type column NO$_2$ products (OMNO2) is available
820 from the NASA Goddard Earth Sciences Data and Information Services Center (GES DISC)
821 website (https://disc.gsfc.nasa.gov/datasets/OMNO2G_003/summary). Other OMNO2-associated

822 NO$_2$ products such as the Level-2 gridded column product, OMNO2G, and the Level-3 gridded

823 column product, OMNO2d, both sampled at regular 0.25° latitude x 0.25° longitude wide grids are

824 distributed   through   the   NASA   GES-DISC

825 (https://disc.gsfc.nasa.gov/datasets/OMNO2d_003/summary)   and   GIOVANNI

826 (https://giovanni.gsfc.nasa.gov/giovanni/) websites. An additional high spatial resolution (0.1° x

827 0.1° latitude-longitude grid) OMNO2d product (OMNO2d_HR) is also made available through

828 the   NASA   AVDC   website

829 (https://avdc.gsfc.nasa.gov/pub/data/satellite/Aura/OMI/V03/L3/OMNO2d_HR/).   The   AVDC

830 website   also   hosts   overpass   files   for   several   hundred   sites   around   the   globe

831 (https://avdc.gsfc.nasa.gov/pub/data/satellite/Aura/OMI/V03/L2OVP/OMNO2/).

832

833 *Author contributions.* LNL, NAK, JJ, and AV designed the data analysis. WQ, ZF, NAK, DH,

834 and AV developed and evaluated the GLER product. EY, SM, AV, NAK, JJ, and BF developed

835 and evaluated the cloud product. LNL, NAK, SM, WHS, and EB have developed and evaluated

836 the NASA NO$_2$ Standard Product. LNL and SC conducted validation of the OMI NO$_2$ products

837 using Pandora and other independent observations. LNL, AV, SM, and ZF wrote the manuscript

838 with comments from all coauthors.

839

840 *Competing interests.* The authors declare no competing interests.

841

842 *Acknowledgements.* We acknowledge the NASA Earth Science Division for funding OMI NO$_2$

843 product development and analysis. The Dutch–Finnish-built OMI instrument is part of the NASA

844 EOS Aura satellite payload. KNMI and the Netherlands Space Agency (NSO) manage the OMI

845 project. We acknowledge the NASA Pandora, ESA-Pandonia, and NASA's DISCOVER-AQ

846 projects for free access to the data. We thank the two anonymous reviewers for their helpful

847 comments.

848
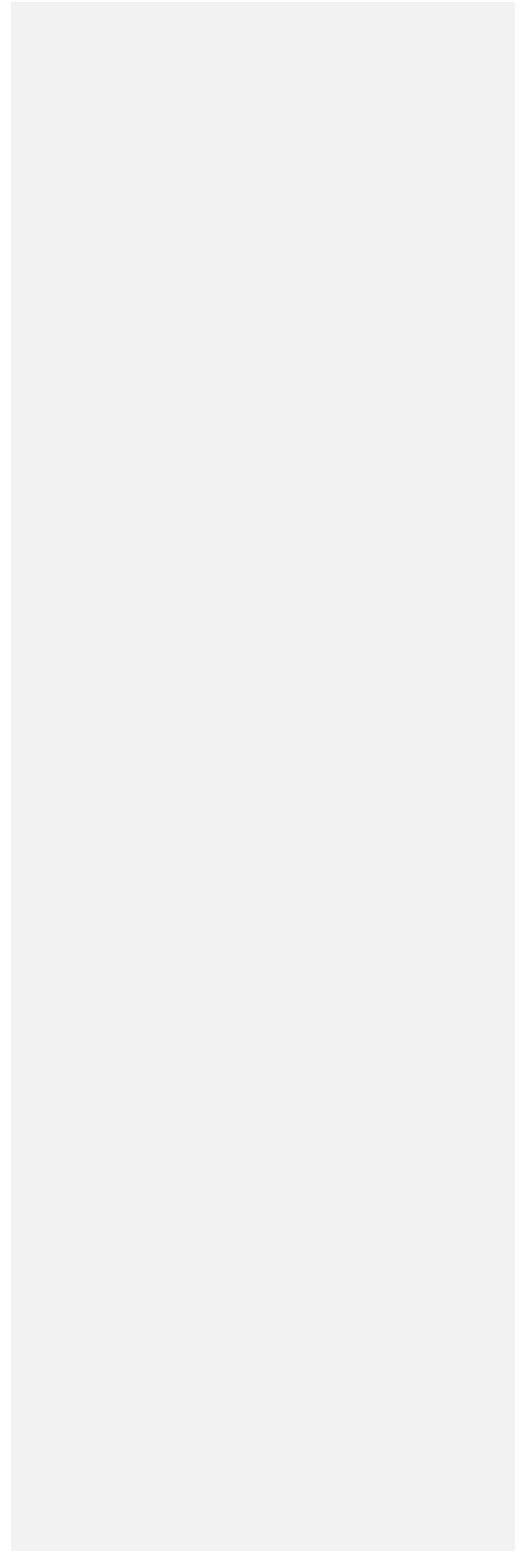
849 **References**

850 Beirle, S., Boersma, K. F., Platt, U., Lawrence, M. G., and Wagner, T.: Megacity emissions and
851   lifetimes of nitrogen oxides probed from space, *Science*, *333*, 1737–1739.
852   https://doi.org/10.1126/science.1207824, 2011.

853 Berezin, E. V, Konovalov, I. B., Ciais, P., Richter, A., Tao, S., Janssens-Maenhout, G., et al.:
854   Multiannual changes of CO_2 emissions in China: indirect estimates derived from satellite
855   measurements of tropospheric NO_2 columns, *Atmos. Chem. Phys*, *13*, 9415–9438.
856   https://doi.org/10.5194/acp-13-9415-2013, 2013.

857 Boersma, K. F., Eskes, H. J., Dirksen, R. J., van der A, R. J., Veefkind, J. P., Stammes, P., Huijnen,
858   V., Kleipool, Q. L., Sneep, M., Claas, J., Leitão, J., Richter, A., Zhou, Y., and Brunner, D.:
859   An improved tropospheric NO_2 column retrieval algorithm for the Ozone Monitoring
860   Instrument, *Atmos. Meas. Tech.*, 4, 1905–1928, https://doi.org/10.5194/amt-4-1905-2011,
861   2011.

862 Boersma, K. F., Eskes, H. J., Richter, A., De Smedt, I., Lorente, A., Beirle, S., van Geffen, J. H.
863   G. M., Zara, M., Peters, E., Van Roozendael, M., Wagner, T., Maasakkers, J. D., van der A,
864   R. J., Nightingale, J., De Rudder, A., Irie, H., Pinardi, G., Lambert, J.-C., and Compernolle,
865   S. C.: Improving algorithms and uncertainty estimates for satellite NO_2 retrievals: results
866   from the quality assurance for the essential climate variables (QA4ECV) project, *Atmos.*
867   *Meas. Tech.*, 11, 6651–6678, https://doi.org/10.5194/amt-11-6651-2018, 2018.

868 Bucsela, E.J., Celarier, E.A., Wenig, M.O., Gleason, J.F., Veefkind, J.P., Boersma, K.F., and
869   Brinksma, E.J.: Algorithm for NO_2 vertical column retrieval from the Ozone Monitoring
870   Instrument, *IEEE Trans. Geosci. Remote Sens.*, 44, 5, 2006.

871 Bucsela, E. J., Krotkov, N. A., Celarier, E. A., Lamsal, L. N., Swartz, W. H., Bhartia, P. K.,
872   Boersma, K. F., Veefkind, J. P., Gleason, J. F., and Pickering, K. E.: A new stratospheric and
873   tropospheric NO_2 retrieval algorithm for nadir-viewing satellite instruments: applications to
874   OMI, *Atmos. Meas. Tech.*, 6, 2607–2626, https://doi.org/10.5194/amt-6-2607-2013, 2013.

875 Cai, K., Li, S., Zheng, F., Yu, C., Zhang, X., Liu, Y., and Li, Y.: Spatio-temporal Variations in
876   NO_2 and $PM_{2.5}$ over the Central Plains Economic Region of China during 2005-2015 Based
877   on Satellite Observations, *Aer. Air Qual. Res.*, 5, 1221–1235,
878   10.4209/aaqr.2017.10.0394, 2018.

879 Canty, T. P., Hembeck, L., Vinciguerra, T. P., Anderson, D. C., Goldberg, D. L., Carpenter, S.

880   F., Allen, D. J., Loughner, C. P., Salawitch, R. J., and Dickerson, R. R.: Ozone and NO_x
881   chemistry in the eastern US: evaluation of CMAQ/CB05 with satellite (OMI) data, *Atmos.*
882   *Chem. Phys.*, 19, 10965–10982, 10.5194/acp-15-10965-2015, 2015.

883 Castellanos, P., and Boersma, K. F.: Reductions in nitrogen oxides over Europe driven by
884   environmental policy and economic recession, *Sci. Rep.*, 1, 10.1038/srep00265, 2012.

885 Celarier, E. A., et al: Validation of Ozone Monitoring Instrument nitrogen dioxide columns, *J.*
886   *Geophys. Res.*, 113, D15S15, doi:10.1029/2007JD008908, 2008.

887 Chance, K., Kurosu, T.P., and Sioris, K.E.: Undersampling correction for array detector-based
888   satellite spectrometers, *Appl. Opt.*, 44, 1296– 1304, 2005.

889 Chan, K. L., Wang, Z., Ding, A., Heue, K.-P., Shen, Y., Wang, J., Zhang, F., Shi, Y., Hao, N., and
890   Wenig, M.: MAX-DOAS measurements of tropospheric NO_2 and HCHO in Nanjing and a
891   comparison to ozone monitoring instrument observations, *Atmos. Chem. Phys.*, 19, 10051–
892   10071, https://doi.org/10.5194/acp-19-10051-2019, 2019.

893 Choi, S., Lamsal, L. N., Follette-Cook, M., Joiner, J., Krotkov, N. A., Swartz, W. H., Pickering,
894   K. E., Loughner, C. P., Appel, W., Pfister, G., Saide, P. E., Cohen, R. C., Weinheimer, A. J.,
895   and Herman, J. R.: Assessment of NO_2 observations during DISCOVER-AQ and KORUS-
896   AQ field campaigns, Atmos. Meas. Tech., 13, 2523–2546, https://doi.org/10.5194/amt-13-
897   2523-2020, 2020.

898 Cooper, M.J., Martin, R.V., Lyapustin, A.I., and McLinden, C.A.: Assessing snow extent data sets
899   over North America to inform and improve trace gas retrievals from solar backscatter, *Atmos.*
900   *Meas. Tech.*, 11, 2983-2994, https://doi.org/10.5194/amt-11-2983-2018, 2018.

901 Cox, C. and Munk, W.: Statistics of the sea surface derived from sun glitter, *J. Mar. Res.*, 13, 198–
902   227, 1954.

903 de Foy, B., Lu, Z., Streets, D. G., Lamsal, L. N., and Duncan, B. N.: Estimates of power plant NO_x
904   emissions and lifetimes from OMI NO_2 satellite retrievals. *Atmos. Environ.*, *116*, 1–11,
905   https://doi.org/10.1016/j.atmosenv.2015.05.056, 2015.

906 Dirksen, R., Dobber, M., Voors, R, and Levelt, P.: Prelaunch characterization of the Ozone
907   Monitoring Instrument transfer function in the spectral domain, *Appl. Opt.*, 45, 3972– 3981,
908   2006.

909 Dix, B., Bruin, J., Roosenbrand, E., Vlemmix, T., Francoeur, C., Gorchov-
910   Negron, A., McDonald, B., Zhizhin, M., Elvidge, C., Veefkind, P., Levelt, P., and de Gouw,

J.: Nitrogen Oxide Emissions from U.S. Oil and Gas Production: Recent Trends and Source Attribution, *Geophys. Res. Lett.*, 1, e2019GL085866, 10.1029/2019gl085866, 2020.

Dobber, M., Kleipool, Q., Dirksen, R., Levelt, P. F., Jaross, G., Taylor, S., et al.: Validation of Ozone Monitoring Instrument level 1b data products. *J. Geophys. Res.*, https://doi.org/10.1029/2007JD008665, 2008.

Douglass, A. R., Stolarski, R.S., Strahan, S.E., and Connell, P.S.: Radicals and reservoirs in the GMI chemistry and transport model: Comparison to measurements, *J. Geophys. Res.*, 109, D16302, doi:10.1029/2004JD004632, 2004.

Duncan, B. N., Yoshida, Y., Foy, B., Lamsal, L. N., Streets, D. G., Lu, Z., Pickering, K. E., and Krotkov, N. A.: The observed response of Ozone Monitoring Instrument (OMI) NO_2 columns to NOx emission controls on power plants in the United States: 2005–2011, *Atmos. Environ.*, 102–111, 10.1016/j.atmosenv.2013.08.068, 2013.

Duncan, B.N., Lamsal, L.N., Thompson, A.M., Yoshida, Y., Lu, Z., Streets, D.G., Hurwitz, M.M., Pickering, K.E.: A space-based, high-resolution view of notable changes in urban NO_x pollution around the world (2005-2014), *J. Geophys. Res.*, 121, 976–996, doi:10.1002/2015JD024121, 2016.

Eskes, H. J. and Boersma, K. F.: Averaging kernels for DOAS total-column satellite retrievals, *Atmos. Chem. Phys.*, 3, 1285–1291, https://doi.org/10.5194/acp-3-1285-2003, 2003.

Fasnacht, Z., Vasilkov, A., Haffner, D., Qin, W., Joiner, J., Krotkov, N., Sayer, A. M., and Spurr, R.: A geometry-dependent surface Lambertian-equivalent reflectivity product for UV–Vis retrievals – Part 2: Evaluation over open ocean, *Atmos. Meas. Tech.*, 12, 6749–6769, https://doi.org/10.5194/amt-12-6749-2019, 2019.

Geddes, J. A. and Martin, R. V.: Global deposition of total reactive nitrogen oxides from 1996 to 2014 constrained with satellite observations of NO_2 columns, *Atmos. Chem. Phys.*, 17, 10071–10091, https://doi.org/10.5194/acp-17-10071-2017, 2017.

Gelaro, R., McCarty, W., Suárez, M.J., Todling, R., Molod, A., Takacs, L., Randles, C.A., Darmenov, A., Bosilovich, M.G., Reichle, R., Wargan, K., Coy, L., Cullather, R., Draper, C., Akella, S., Buchard, V., Conaty, A., da Silva, A.M., Gu, W., Kim, G., Koster, R., Lucchesi, R., Merkova, D., Nielsen, J.E., Partyka, G., Pawson, S., Putman, W., Rienecker, M., Schubert, S.D., Sienkiewicz, M., and Zhao, B.: The Modern-Era Retrospective Analysis for Research and Applications, Version 2 (MERRA-2). *J. Climate,* 30, 5419–

942 5454, https://doi.org/10.1175/JCLI-D-16-0758.1, 2017.

943 Ghude, S.   D., Kulkarni, S.   H., Jena, C., Pfister, G.   G., Beig, G., Fadnavis, S.,   and A, R.

944   J.: Application of satellite observations for identifying regions of dominant sources of

945   nitrogen   oxides   over   the   Indian   Subcontinent, *J.   Geophys.   Res.*, 2, 1075–

946   1089, 10.1029/2012jd017811, 2013.

947 Goldberg, D. L., Lamsal, L. N., Loughner, C. P., Swartz, W. H., Lu, Z., and Streets, D. G.: A high-

948   resolution and observationally constrained OMI NO_2 satellite retrieval. *Atmos. Chem. Phys.*,

949   *17*, 11403–11421. https://doi.org/10.5194/acp-17-11403-2017, 2017.

950 Goldberg, D. L., Saide, P. E., Lamsal, L. N., de Foy, B., Lu, Z., Woo, J.-H., et al.: A top-down

951   assessment using OMI NO_2 suggests an underestimate in the NO_x emissions inventory in

952   Seoul, South Korea, during KORUS-AQ. *Atmos. Chem. Phys.*, *19*, 1801–1818.

953   https://doi.org/10.5194/acp-19-1801-2019, 2019a.

954 Goldberg, D., Lu, Z., Oda, T., Lamsal, L.N, Liu, F., Griffin, D., McLinden, C., Krotkov, N.A.,

955   Duncan, B.N., Streets, D.: Exploiting OMI NO_2 satellite observations to infer fossil-fuel CO_2

956   emissions   from   U.S.   megacities,   *Sci.   Tot.   Environ.*,   695,   133805,

957   10.1016/j.scitotenv.2019.133805, 2019b.

958 Gu, J., Chen, L., Yu, C., Li, S., Tao, J., Fan, M., Xiong, X., Wang, Z., Shang, H.,

959   and Su, L.: Ground-Level NO_2 Concentrations over China Inferred from the Satellite OMI

960   and CMAQ Model Simulations, *Rem. Sens.*, 6, 519, 10.3390/rs9060519, 2017.

961 Han, K., Lee, C., Lee, J., Kim, J., and Song, C.: A comparison study between model-predicted

962   and OMI-retrieved tropospheric NO_2 columns over the Korean peninsula, *Atmos.*

963   *Environ.*, 17, 2962–2971, 10.1016/j.atmosenv.2010.10.016, 2011.

964 Herman, J., Cede, A., Spinei, E., Mount, G., Tzortziou, M., and Abuhassan, N.: NO_2 column

965   amounts from ground-based Pandora and MFDOAS spectrometers using the direct-sun

966   DOAS technique: Intercomparisons and application to OMI validation, *J. Geophys. Res.*

967   *Atmos.*,   114,   D13,   https://doi.org/10.1029/2009JD011848,

968   https://agupubs.onlinelibrary.wiley.com/doi/abs/10.1029/2009JD011848, 2009.

969 Herman, J., Spinei, E., Fried, A., Kim, J., Kim, J., Kim, W., Cede, A., Abuhassan, N., and Segal-

970   Rozenhaimer, M.: NO_2 and HCHO measurements in Korea from 2012 to 2016 from Pandora

971   spectrometer instruments compared with OMI retrievals and with aircraft measurements

972   during   the   KORUS-AQ   campaign,   *Atmos.   Meas.   Tech.*,   11,   4583–4603,

973   https://doi.org/10.5194/amt-11-4583-2018,   https: //www.atmos-meas-
974   tech.net/11/4583/2018/, 2018.

975   Herron-Thorpe, F. L., Lamb, B. K., Mount, G. H., and Vaughan, J. K.: Evaluation of a regional air
976   quality forecast model for tropospheric NO_2 columns using the OMI/Aura satellite
977   tropospheric NO_2 product, *Atmos. Chem. Phys.*, 18, 8839–8854, 10.5194/acp-10-8839-
978   2010, 2010.

979   Hudman, R. C., Moore, N. E., Mebust, A. K., Martin, R. V., Russell, A. R., Valin, L. C.,
980   and Cohen, R. C.: Steps towards a mechanistic model of global soil nitric oxide emissions:
981   implementation and space based-constraints, *Atmos. Chem. Phys.*, 16, 7779–
982   7795, 10.5194/acp-12-7779-2012, 2012.

983   Ialongo, I., Herman, J., Krotkov, N., Lamsal, L., Boersma, K. F., Hovila, J., and Tamminen, J.:
984   Comparison of OMI NO_2 observations and their seasonal and weekly cycles with ground-
985   based measurements in Helsinki, *Atmos. Meas. Tech.*, 10, 5203–5212, 10.5194/amt-9-5203-
986   2016, 2016.

987   Joiner, J., Bhartia, P., Cebula, R., Hilsenrath, E., McPeters, R., and Park, H.: Rotational Raman
988   scattering (Ring effect) in satellite backscatter ultraviolet measurements, *Appl. Opt.*, 34,
989   4513-4525, 1995.

990   Joiner J. and Vasilkov, A. P.: First Results from the OMI Rotational-Raman Scattering Cloud
991   Pressure Algorithm, *IEEE Trans. Geophys. Remote Sens.,* 44, 1272–1282, 2006.

992   Joiner, J., Vasilkov, A. P., Gupta, P., Bhartia, P. K., Veefkind, P., Sneep, M., de Haan, J., Polonsky,
993   I., and Spurr, R.: Fast simulators for satellite cloud optical centroid pressure retrievals;
994   evaluation of OMI cloud retrievals, *Atmos. Meas. Tech.*, 5, 529–545,
995   https://doi.org/10.5194/amt-5-529-2012, 2012.

996   Judd, L. M., Al-Saadi, J. A., Janz, S. J., Kowalewski, M. G., Pierce, R. B., Szykman, J. J., Valin,
997   L. C., Swap, R., Cede, A., Mueller, M., Tiefengraber, M., Abuhassan, N., and Williams, D.:
998   Evaluating the impact of spatial resolution on tropospheric NO_2 column comparisons within
999   urban areas using high-resolution airborne data, *Atmos. Meas. Tech.,* 12, 6091–6111,
1000   https://doi.org/10.5194/amt-12-6091-2019, 2019.

1001   Kim, H. C., Lee, P., Judd, L., Pan, L., and Lefer, B.: OMI NO_2 column densities over North
1002   American urban cities: the effect of satellite footprint resolution, *Geos. Mod. Develop.*, 3,
1003   1111–1123, 10.5194/gmd-9-1111-2016, 2016.

Kleipool, Q. L., Dobber, M. R., de Haan, J. F., and Levelt, P. F.: Earth surface reflectance climatology from 3 years of OMI data, *J. Geophys. Res.*, 113, D18308, doi:10.1029/2008JD010290, 2008.

Koelemeijer, R. B. A., Stammes, P., Hovenier, J. W., and de Haan, J. F.: A fast method for retrieval of cloud parameters using oxygen A-band measurements from the Global Ozone Monitoring Experiment, *J. Geophys. Res.,* 106, 3475–3496, 2001.

Konovalov, I. B., Berezin, E. V., Ciais, P., Broquet, G., Zhuravlev, R. V., and Janssens-Maenhout, G.: Estimation of fossil-fuel CO_2 emissions using satellite measurements of "proxy" species. *Atmos. Chem. Phys.*, *16*(21), 13509–13540. https://doi.org/10.5194/acp-16-13509-2016, 2016.

Krotkov, N. A., McLinden, C. A., Li, C., Lamsal, L. N., Celarier, E. A., Marchenko, S. V., Swartz, W. H., Bucsela, E. J., Joiner, J., Duncan, B. N., Boersma, K..F., Pepijn, J.P., Levelt, P.F., Fioletov, V.E., Dickerson, R. R., He, H., Lu, Z., and D. G. Streets, D.G.: Aura OMI observations of regional SO_2 and NO_2 pollution changes from 2005 to 2015, *Atmos. Chem. Phys.*, 7, 4605–4629, 10.5194/acp-16-4605-2016, 2016.

Krotkov, N. A., Lamsal, L. N., Celarier, E. A., Swartz, W. H., Marchenko, S. V., Bucsela, E. J., et al.: The version 3 OMI NO_2 standard product. *Atmos. Meas. Tech.*, *10*, 3133–3149. https://doi.org/10.5194/amt-10-3133-2017, 2017.

Kuhlmann, G., Lam, Y. F., Cheung, H. M., Hartl, A., Fung, J. C. H., Chan, P. W., and Wenig, M. O.: Development of a custom OMI NO_2 data product for evaluating biases in a regional chemistry transport model, *Atmos. Chem. Phys*., 15, 5627–5644, https://doi.org/10.5194/acp-15-5627-2015, 2015.

Lamsal, L.N., Martin, R.V., van Donkelaar, A., Celarier, E.A., Bucsela, E.J., Boersma, K.F., Dirksen, R., Luo, C., and Wang, Y.: Indirect validation of tropospheric nitrogen dioxide retrieved from the OMI satellite instrument: Insight into the seasonal variation of nitrogen oxides at northern midlatitude, *J. Geophys. Res*., 115, doi:10.1029/2009JD013351, 2010.

Lamsal, L.N., Martin, R.V., Parrish D.D., and Krotkov, N.A.: Scaling relationship for NO_2 pollution and population size: A satellite perspective, *Environ. Sci. Technol*, 47, 7855-7861, 2013.

Lamsal, L. N., Krotkov, N. A., Celarier, E. A., Swartz, W. H., Pickering, K. E., Bucsela, E. J., Gleason, J. F., Martin, R. V., Philip, S., Irie, H., Cede, A., Herman, J., Weinheimer, A.,

Szykman, J. J., and Knepp, T. N.: Evaluation of OMI operational standard NO_2 column retrievals using in situ and surface-based NO_2 observations, *Atmos. Chem. Phys.*, 14, 11587–11609, https://doi.org/10.5194/acp-14-11587-2014, 2014.

Lamsal, L.N., Duncan, B.N., Yoshida, Y., Krotkov, N.A., Pickering, K.E., Streets, D.G., Lu, Z.: U.S. NO_2 trends (2005–2013): EPA Air Quality System (AQS) data versus improved observations from the Ozone Monitoring Instrument (OMI), *Atmos. Env.*, 110, pp:130-143, doi:10.1016/j.atmosenv.2015.03.055, 2015.

Laughner, J. L., Zhu, Q., and Cohen, R. C.: Evaluation of version 3.0B of the BEHR OMI NO_2 product. *Atmos. Meas. Tech.*, *12*, 129–146. https://doi.org/10.5194/amt-12-129-2019, 2019.

Laughner, J.J. and Cohen, R.C.: Direct observation of changing NO_x lifetime in North American cities, *Science,* 366, 6466, pp. 723-727, doi: 10.1126/science.aax6832, 2019.

Levelt, P. F., van den Oord, G. H. J., Dobber, M. R., Dirksen, R. J., Malkki, A., Visser, H., de Vries, J., and Stammes, P.: The ozone monitoring instrument. *IEEE Trans. Geosci. Remote Sens.*, *44*(5), 1093–1101. https://doi.org/Urn:nbn:nl:ui:25-648485, 2006.

Levelt, P. F., Joiner, J., Tamminen, J., Veefkind, J. P., Bhartia, P. K., Stein Zweers, D. C., Duncan, B. N., Streets, D. G., Eskes, H., van der A, R., McLinden, C., Fioletov, V., Carn, S., de Laat, J., DeLand, M., Marchenko, S., McPeters, R., Ziemke, J., Fu, D., Liu, X., Pickering, K., Apituley, A., González Abad, G., Arola, A., Boersma, F., Chan Miller, C., Chance, K., de Graaf, M., Hakkarainen, J., Hassinen, S., Ialongo, I., Kleipool, Q., Krotkov, N., Li, C., Lamsal, L., Newman, P., Nowlan, C., Suleiman, R., Tilstra, L. G., Torres, O., Wang, H., and Wargan, K.: The Ozone Monitoring Instrument: overview of 14 years in space, *Atmos. Chem. Phys.*, 18, 5699–5745, https://doi.org/10.5194/acp-18-5699-2018, 2018.

Lin, J.-T., Martin, R. V., Boersma, K. F., Sneep, M., Stammes, P., Spurr, R., Wang, P., Van Roozendael, M., Clémer, K., and Irie, H.: Retrieving tropospheric nitrogen dioxide from the Ozone Monitoring Instrument: effects of aerosols, surface reflectance anisotropy, and vertical profile of nitrogen dioxide, *Atmos. Chem. Phys.*, 14, 1441–1461, https://doi.org/10.5194/acp-14-1441-2014, 2014.

Lin, J.-T., Liu, M.-Y., Xin, J.-Y., Boersma, K. F., Spurr, R., Martin, R., and Zhang, Q.: Influence of aerosols and surface reflectance on satellite NO_2 retrieval: seasonal and spatial characteristics and implications for NO_x emission constraints, *Atmos. Chem. Phys.*, 15, 11217-11241, doi:10.5194/acp-15-11217-2015, 2015.

Liu, F., Duncan, B. N., Krotkov, N. A., Lamsal, L. N., Beirle, S., Griffin, D., McLinden, C. A., Goldberg, D. L., and Lu, Z.: A methodology to constrain carbon dioxide emissions from coal-fired power plants using satellite observations of co-emitted nitrogen dioxide, *Atmos. Chem. Phys.*, 20, 99–116, https://doi.org/10.5194/acp-20-99-2020, 2020.

Liu, M.-Y., Lin, J.-T., Boersma, K. F., Pinardi, G., Wang, Y., Chimot, J., Wagner, T., Xie, P., Eskes, H., Van Roozendael, M., Hendrick, F., Wang, P., Wang, T., Yan, Y.-Y., Chen, L.-L., and Ni, R.-J.: Improved aerosol correction for OMI tropospheric NO_2 retrieval over East Asia: constraint from CALIOP aerosol vertical profile, *Atmos. Meas. Tech.*, 12, 1-21, doi:10.5194/amt-12-1-2019, 2019.

Lu, Z., Streets, D. G., de Foy, B., Lamsal, L. N., Duncan, B. N., and Xing, J.: Emissions of nitrogen oxides from US urban areas: Estimation from Ozone Monitoring Instrument retrievals for 2005-2014, *Atmos. Chem. Phys.*, *15*(18), 10367–10383. https://doi.org/10.5194/acp-15-10367-2015, 2015.

Lucht, W., Schaaf, C. B., and Strahler, A. H.: An algorithm for the retrieval of albedo from space using semiempirical BRDF models, *IEEE Trans. Geosci. Remote Sens.*, 38, 977–998, 2000.

Marchenko, S., Krotkov, N. A., Lamsal, L. N., Celarier, E. A., Swartz, W. H., and Bucsela, E. J.: Revising the slant column density retrieval of nitrogen dioxide observed by the Ozone Monitoring Instrument, *J. Geophys. Res.*, 120, 5670--5692, 2015.

Martin, R. V., Chance, K., Jacob., D.J., Kurosu, T.P., Spurr., R.J.D., Bucsela, E., Gleason, J.F., Palmer, P.I., Bey, I., Fiore, A.M., Li, Q., Yantosca, R.M., Koelemeijer, R.B.A.: An improved retrieval of tropospheric nitrogen dioxide from GOME, *J. Geophys. Res.*, 107, 4437, doi:10.1029/2001JD001027, 2002.

McLinden, C. A., Fioletov, V. E., Boersma, K. F., Kharol, S. K., Krotkov, N., Lamsal, L., et al.: Improved satellite retrievals of NO_2 and SO_2 over the Canadian oil sands and comparisons with surface measurements. *Atmos. Chem. Phys.*, *14*, 3637–3656. https://doi.org/10.5194/acp-14-3637-2014, 2014.

Mishchenko, M. I. and Travis, L. D.: Satellite retrieval of aerosol properties over the ocean using polarization as well as intensity of reflected sunlight, *J. Geophys. Res.*, 102, 16989–17013, https://doi.org/10.1029/96JD02425, 1997.

Miyazaki, K., Eskes, H., Sudo, K., Boersma, K. F., Bowman, K., and Kanaya, Y.: Decadal changes in global surface NO_x emissions from multi-constituent satellite data

1097   assimilation, *Atmos. Chem. Phys.*, 2, 807–837, 10.5194/acp-17-807-2017, 2017.

1098   Montgomery, A., and Holloway, T.: Assessing the relationship between satellite-derived NO_2 and

1099   economic growth over the 100 most populous global cities, *J. Appl. Rem.*

1100   *Sens.*, 04, 1, 10.1117/1.jrs.12.042607, 2018.

1101   Morel, A.: Optical modeling of the upper ocean in relation to its biogeneous matter content (Case

1102   I waters), *J. Geophys. Res.,* 93, 10749–10768, https://doi.org/10.1029/JC093iC09p10749,

1103   1988.

1104   National Geophysical Data Center, 2006. 2-minute Gridded Global Relief Data (ETOPO2) v2.

1105   National Geophysical Data Center, NOAA. doi:10.7289/V5J1012Q [access

1106   date:2017/05/22].

1107   Nolin, A., Armstrong, R., and Maslanik, J.: Near real-time SSM/I EASE-grid daily global ice

1108   concentration and snow extent, Digit, Media, Natl. Snow Ice Data Center, Boulder, CO, USA,

1109   2005.

1110   Nowlan, C. R., Martin, R.V., Philip, S., Lamsal, L.N., Krotkov, N.A., Marais, E.A., Wang, S., and

1111   Zhang, Q.: Global dry deposition of nitrogen dioxide and sulfur fioxide inferred from space-

1112   based measurements, *Global Biogeochem. Cycles,* 28, 10, doi: 10.1002/2014GB004805,

1113   2014.

1114   Nowlan, C. R., Liu, X., Leitch, J. W., Chance, K., González Abad, G., Liu, C., Zoogman, P., Cole,

1115   J., Delker, T., Good, W., Murcray, F., Ruppert, L., Soo, D., Follette-Cook, M. B., Janz, S. J.,

1116   Kowalewski, M. G., Loughner, C. P., Pickering, K. E., Herman, J. R., Beaver, M. R., Long,

1117   R. W., Szykman, J. J., Judd, L. M., Kelley, P., Luke, W. T., Ren, X., and Al-Saadi, J. A.:

1118   Nitrogen dioxide observations from the Geostationary Trace gas and Aerosol Sensor

1119   Optimization (GeoTASO) airborne instrument: Retrieval algorithm and measurements during

1120   DISCOVER-AQ Texas 2013, *Atmos. Meas. Tech.*, 9, 2647–2668,

1121   https://doi.org/10.5194/amt-9-2647-2016, 2016.

1122   Palmer, P. I., Jacob, D. J., Fiore, A. M., and Martin, R. V., Air mass factor formulation for

1123   spectroscopic measurements from satellites: Application to formaldehyde retrievals from the

1124   Global Ozone Monitoring Experiment, *J. Geophys. Res.*, 106, 14539–

1125   514550, https://doi.org/10.1029/2000JD900772, 2001.

1126   Pickering, K.E., Bucsela, E., Allen, D., Ring, A., Holzworth, R., and Krotkov, N.A.: Estimates of

1127   lightning NO_x production based on OMI NO_2 observations over the Gulf of Mexico, *J.*

1128  *Geophys. Res.,* 121, 14, pp 8668-8691, DOI: 10.1002/2015JD024179, 2016.

1129 Platt, U., and Stutz, J.: Differential optical absorption spectroscopy (DOAS), principle and

1130  applications, Springer Verlag, Heidelberg, 2006.

1131 Pope, R. J., Chipperfield, M. P., Savage, N. H., Ordóñez, C., Neal, L. S., Lee, L. A., Dhomse, S.

1132  S., Richards, N. A. D., and Keslake, T. D.: Evaluation of a regional air quality model using

1133  satellite column NO_2: treatment of observation errors and model boundary conditions and

1134  emissions, *Atmos. Chem. Phys*., 15, 5611–5626, https://doi.org/10.5194/acp-15-5611-2015,

1135  2015.

1136 Qin, W., Fasnacht, Z., Haffner, D., Vasilkov, A., Joiner, J., Krotkov, N., Fisher, B., and Spurr, R.:

1137  A geometry-dependent surface Lambertian-equivalent reflectivity product for UV–Vis

1138  retrievals – Part 1: Evaluation over land surfaces using measurements from OMI at 466 nm,

1139  *Atmos. Meas. Tech*., 12, 3997–4017, https://doi.org/10.5194/amt-12-3997-2019, 2019.

1140 Rasool, Q. Z., Zhang, R., Lash, B., Cohan, D. S., Cooter, E. J., Bash, J. O., and Lamsal, L.

1141  N.: Enhanced representation of soil NO emissions in the Community Multiscale Air Quality

1142  (CMAQ) model version 5.0.2, *Geosci. Mod. Develop.*, 9, 3177–3197, 10.5194/gmd-9-3177-

1143  2016, 2016.

1144 Ridley, B. A. and Grahek, F. E.: A small, low flow, high sensitivity reaction vessel for NO

1145  chemiluminescence detectors, *J. Atmos. Oceanic Technol.*, 7, 307–311,

1146  https://doi.org/10.1175/1520-0426(1990)0072.0.CO, 1990.

1147 Rienecker, M. M., Suarez, M. J., Gelaro, R., Todling, R., Bacmeister, J., Liu, E., Bosilovich, M.

1148  G., Schubert, S. D., Takacs, L., Kim, G.-K., Bloom, S., Chen, J., Collins, D., Conaty, A., da

1149  Silva, A., Gu, W., Joiner, J., Koster, R. D., Lucchesi, R., Molod, A., Owens, T., Pawson, S.,

1150  Pegion, P., Redder, C. R., Reichle, R., Robertson, F. R., Ruddick, A. G., Sienkiewicz, M.,

1151  and Woollen, J.: MERRA: NASA's Modern-Era Retrospective Analysis for Research and

1152  Applications, *J. Clim.*, 24, 3624–3648, https://doi.org/10.1175/JCLI-D-11-00015.1, 2011.

1153 Rothman, L. S., Gordon., I.E., Barbe, A., Chris Benner, D., Bernath, P.F., Birk, M., Boudon, V.,

1154  Brown, L.R., Campargue, A., Champion, J.-P., Chance, K., Coudert, L.H., Dana, V., Devi,

1155  V.M., Fally, S., Flaud, J.-M., Gamache, R.R., Goldman, A., Jacquemart, D., Kleiner, I.,

1156  Lacome, N., Lafferty, W.J., Mandin, J.-Y., Massie, S.T., Mikhailenko, S.N., Miller, E.E.,

1157  Moazzen-Ahmad, N., Naumenko, O.V., Nikitin, A.V., Orphal, J., Perevalov, V.I., Perrin, A.,

1158  Predoi-Cross, A., Rinsland, C.P., Rotger, M., Šimečková, M., Smith, M.A.H., Sung, K.,

1159   Tashkun, S.A., Tennyson, J., Toth, R.A., Vandaele, A.C., Vander Auwera, J.: The HITRAN
1160   2008 molecular spectroscopic database, *J. Quant. Spectrosc. Radiat. Trans.*, 114, 533– 572,
1161   2009.

1162 Russell, A. R., Perring, A. E., Valin, L. C., Bucsela, E. J., Browne, E. C., Wooldridge, P. J., and
1163   Cohen, R. C.: A high spatial resolution retrieval of NO_2 column densities from OMI: method
1164   and evaluation, *Atmos. Chem. Phys.*, 11, 8543–8554, https://doi.org/10.5194/acp-11-8543-
1165   2011, 2011.

1166 Schaaf, C. B., Gao, F., Strahler, A. H., Lucht, W., Li, X., Tsang, T., Strugnell, N. C., Zhang, X.,
1167   Jin, Y., Muller, J.-P., Lewis, P., Barnsley, M., Hobson, P., Disney, M., Roberts, G.,
1168   Dunderdale, M., Doll, C., d'Entremont, R., Hu, B., Liang, S., and Privette, J. L.: First
1169   operational BRDF, albedo and nadir reflectance products from MODIS, *Rem. Sens. Environ.*,
1170   83, 135–148, 2002.

1171 Schaaf, C. L. B., Liu, J., Gao, F., and Strahler, A. H.: MODIS albedo and reflectance anisotropy
1172   products from Aqua and Terra, in: Land Remote Sensing and Global Environmental Change:
1173   NASA's Earth Observing System and the Science of ASTER and MODIS, Remote Sensing
1174   and Digital Image Processing Series, edited by: Ramachandran, B., Justice, C., and Abrams,
1175   M., Vol. 11, Springer-Verlag, New York, 873 pp., 2011.

1176 Schenkeveld, V. M. E., Jaross, G., Marchenko, S., Haffner, D., Kleipool, Q. L., Rozemeijer, N.
1177   C., Veefkind, J. P., and Levelt, P. F.: In-flight performance of the Ozone Monitoring
1178   Instrument, *Atmos. Meas. Tech.,* 10, 1957–1986, https://doi.org/10.5194/amt-10-1957-2017,
1179   2017.

1180 Schreier, S. F., Richter, A., Kaiser, J. W., and Burrows, J. P.: The empirical relationship between
1181   satellite-derived tropospheric NO_2 and fire radiative power and possible implications for fire
1182   emission rates of NO_x, *Atmos. Chem. Phys.*, 5, 2447–2466, 10.5194/acp-14-2447-2014, 2014.

1183 Shah, V., Jacob, D. J., Li, K., Silvern, R. F., Zhai, S., Liu, M., Lin, J., and Zhang, Q.: Effect of
1184   changing NO_x lifetime on the seasonality and long-term trends of satellite-observed
1185   tropospheric NO_2 columns over China, *Atmos. Chem. Phys. Disc.*, 1–23, 10.5194/acp-2019-
1186   670, 2019.

1187 Spurr, R. J. D.: VLIDORT: a linearized pseudo-spherical vector discrete ordinate radiative transfer
1188   code for forward model and retrieval studies in multilayer multiple scattering media, *J. Quant.*
1189   *Spectrosc. Rad. Trans.,* 102, 316–421, https://doi.org/10.1016/j.jqsrt.2006.05.005, 2006.

Stammes, P., Sneep, M., de Haan, J. F., Veefkind, J. P., Wang, P., and Levelt, P. F.: Effective cloud fractions from the Ozone Monitoring Instrument: Theoretical framework and validation, *J. Geophys. Res.,* 113, D16S38, https://doi.org/10.1029/2007JD008820, 2008.

Strahan, S. E., Duncan, B.N., and Hoor, P.: Observationally derived transport diagnostics for the lowermost stratosphere and their application to the GMI chemistry and transport model, *Atmos. Chem. Phys.*, **7**, 2435– 2445, 2007.

Strode, S.A., Rodriguez, J.M., Logan, J.A., Cooper, O.R., Witte, J.C., Lamsal, L.N., Damon, M., Van Aartsen, B., Steenrod, S.D., and Strahan, S.E.:Trends and variability in surface ozone over the United States, *J. Geophys. Res.*, doi: 10.1002/2014JD022784, 2015.

Tang, W., Cohan, D. S., Pour-Biazar, A., Lamsal, L. N., White, A. T., Xiao, X., Zhou, W., Henderson, B. H., and Lash, B. F.: Influence of satellite-derived photolysis rates and NO_x emissions on Texas ozone modeling, *Atmos. Chem. Phys.*, 4, 1601–1619, 10.5194/acp-15-1601-2015, 2015.

Thalman, R., and Volkamer, R.: Temperature dependent absorption cross-sections of O_2-O_2 collision pairs between 340 and 630 nm and at atmospherically relevant pressure, *Phys. Chem. Chem. Phys.*, 15, 15371–15381, https://doi.org/10.1039/C3CP50968K, 2013.

Thornton, J. A., Wooldridge, P. J., and Cohen, R. C.: Atmospheric NO_2: in situ laser-induced fluorescence detection at parts per trillion mixing ratios, *Anal. Chem.*, 72, 528–539, https://doi.org/10.1021/ac9908905, https://doi.org/10.1021/ac9908905, 2000.

Tong, D., Lamsal, L.N., Pan, L., Kim, H., Lee, P., Chai, T., Pickering, K.E.: Long-term NO_x trends over large cities in the United States during the Great Recession: Intercomparison of satellite retrievals, ground observations, and emission inventories, *Atmos. Env.,* 109, doi: 10.1016/j.atmosenv.2015.01.035, 2015.

Torres, O., Tanskanen, A., Veihelman, B., Ahn, C., Braak, R., Bhartia, P. K., Veefkind, V., and Levelt, P.: Aerosols and Surface UV Products from OMI Observations: An Overview, *J. Geophys. Res.*, 112, D24S47, https://doi.org/10.1029/2007JD008809, 2007.

van der A, R. J., Eskes, H.J., Boersma, K.F., van Noije, T.P.C., Van Roozendael, M., De Smedt, I., Peters, D. H. M. U., and Meijer E.W.: Identification of NO_2 sources and their trends from space using seasonal variability analyses, *J. Geophys. Res.*, 113, D04302, doi:10.1029/2007JD009021, 2008.

van Geffen, J. H. G. M., Boersma, K. F., Van Roozendael, M., Hendrick, F., Mahieu, E., De Smedt,

I., Sneep, M., and Veefkind, J. P.: Improved spectral fitting of nitrogen dioxide from OMI in the 405–465 nm window, *Atmos. Meas. Tech.*, 8, 1685–1699, https://doi.org/10.5194/amt-8-1685-2015, 2015.

Vandaele, A. C., Hermans, C., Simon, P.C., Carleer, M., Colin, R., Fally, S., Mérienne, M.F., Jenouvrier, A., and Coquart, B.: Measurements of the NO_2 absorption cross-section from 42,000 cm^{-1} to 10,000 cm^{-1} (238-1000 nm) at 220 K and 294 K, *J. Quant. Spectrosc. Radiat. Trans.*, 59, 171– 184, 1998.

Vasilkov, A., Joiner, J., Gleason, J., and Bhartia, P.K.: Ocean Raman scattering in satellite backscatter UV measurements, *Geophys. Res. Lett.*, 29, 1837, doi:10.1029/2002GL014955, 2002.

Vasilkov, A. P., Herman, J. R., Ahmad, Z., Karu, M., and Mitchell, B. G.: Assessment of the ultraviolet radiation field in ocean waters from space-based measurements and full radiative-transfer calculations, *Appl. Opt.,* 44, 2863–2869, https://doi.org/10.1364/AO.44.002863, 2005.

Vasilkov, A.P., Joiner, J., Spurr, R., Bhartia, P.K., Levelt, P., Stephens, G.: Evaluation of the OMI cloud pressures derived from rotational Raman scattering by comparisons with other satellite data and radiative transfer simulations, *J. Geophys. Res*., 113, d15, https://doi.org/10.1029/2007JD008689, 2008.

Vasilkov, A. P., Joiner, J., Haffner, D., Bhartia, P. K., and Spurr, R. J. D.: What do satellite backscatter ultraviolet and visible spectrometers see over snow and ice? A study of clouds and ozone using the A-train, *Atmos. Meas. Tech.*, 3, 619–629, https://doi.org/10.5194/amt-3-619-2010, 2010.

Vasilkov, A., Qin, W., Krotkov, N., Lamsal, L., Spurr, R., Haffner, D., Joiner, J., Yang, E.-S., and Marchenko, S.: Accounting for the effects of surface BRDF on satellite cloud and trace-gas re- trievals: a new approach based on geometry-dependent Lambertian equivalent reflectivity applied to OMI algorithms, *Atmos. Meas. Tech*., 10, 333–349, https://doi.org/10.5194/amt-10-333-2017, 2017.

Vasilkov, A., Yang, E.-S., Marchenko, S., Qin, W., Lamsal, L., Joiner, J., Krotkov, N., Haffner, D., Bhartia, P.K., Spurr, R.: A cloud algorithm based on the O_2-O_2 477 nm absorption band featuring an advanced spectral fitting method and the use of surface geometry-dependent Lambertian-equivalent reflectivity, *Atmos. Meas. Tech*., 11, 4093-4107, doi: 10.5194/amt-11-

4093-2018, 2018.

Vasilkov, A., Krotkov, N., Yang, E.-S., Lamsal, L., Joiner, J., Castellanos, P., Fasnacht, Z., and Spurr, R.: Explicit and consistent aerosol correction for visible wavelength satellite cloud and nitrogen dioxide retrievals based on optical properties from a global aerosol analysis, *Atmos. Meas. Tech. Discuss.*, https://doi.org/10.5194/amt-2019-458, in review, 2020.

Veefkind J. P., de Haan, J. F., Brinksma, E. J., Kroon, M., and Levelt, P. F.: Total ozone from the Ozone Monitoring Instrument (OMI) using the DOAS technique, *IEEE Trans. Geophys. Remote Sens.*, 44, 1239–1244, 2006.

Veefkind, J. P., de Haan, J. F., Sneep, M., and Levelt, P. F.: Improvements to the OMI O_2– O_2 operational cloud algorithm and comparisons with ground-based radar–lidar observations, *Atmos. Meas. Tech.*, 9, 6035–6049, https://doi.org/10.5194/amt-9-6035-2016, 2016.

Vinken, G. C. M., Boersma, K. F., Donkelaar, A., and Zhang, L., Constraints on ship NO_x emissions in Europe using GEOS-Chem and OMI satellite NO_2 observations, *Atmos. Chem. Phys.*, 3, 1353–1369, 10.5194/acp-14-1353-2014, 2014a.

Vinken, G. C. M., Boersma, K. F., Maasakkers, J. D., Adon, M., and Martin, R. V.: Worldwide biogenic soil NO_x emissions inferred from OMI NO_2 observations, *Atmos. Chem. Phys.*, 18, 10363–10381, 10.5194/acp-14-10363-2014, 2014b.

Volkamer, R., Spietz, P., Burrows, J.P., and Platt, U., High-resolution absorption cross-section of Glyoxal in the UV/VIS and IR spectral ranges, *J. Photochem. Photobiol.*, **172**, 35– 46, doi:10.1016/j.jphotochem.2004.11.011, 2005.

Meissner, T. and Wentz, F.J.: The Complex Dielectric Constant of Pure and Sea Water from Microwave Satellite Observations. *IEEE Trans. Geo. Rem. Sens.*, 42, 1836-1849. http://dx.doi.org/10.1109/TGRS.2004.831888, 2004.

Wentz, F., Hilburn, K., and Smith, K.: RSS SSMIS ocean product grids daily from DMSP F16 NETCDF. Dataset available online from the NASA Global Hydrology Resource Center DAAC, Huntsville, Alabama, USA, https://doi.org/10.5067/MEASURES/DMSP-F16/SSMIS/DATA301, 2012.

Zara, M., Boersma, K. F., De Smedt, I., Richter, A., Peters, E., van Geffen, J. H. G. M., Beirle, S., Wagner, T., Van Roozendael, M., Marchenko, S., Lamsal, L. N., and Eskes, H. J.: Improved slant column density retrieval of nitrogen dioxide and formaldehyde for OMI and GOME-2A from QA4ECV: intercomparison, uncertainty characterisation, and trends, *Atmos. Meas.*

1283   *Tech.*, 11, 4033–4058, https://doi.org/10.5194/amt-11-4033-2018, 2018.

1284   Zhou, Y., Brunner, D., Spurr, R. J. D., Boersma, K. F., Sneep, M., Popp, C., and Buchmann, B.:

1285   Accounting for surface reflectance anisotropy in satellite retrievals of tropospheric NO_2,

1286   *Atmos. Meas. Tech.*, 3, 1185–1203, https://doi.org/10.5194/amt-3-1185-2010, 2010.

1287   Zhou, Y., Brunner, D., Hueglin, C., Henne, S., and Staehelin, J.: Changes in OMI tropospheric

1288 NO_2 columns over Europe from 2004 to 2009 and the influence of meteorological

1289   variability, *Atmos. Environ.*, 482–495, 10.1016/j.atmosenv.2011.09.024, 2012.
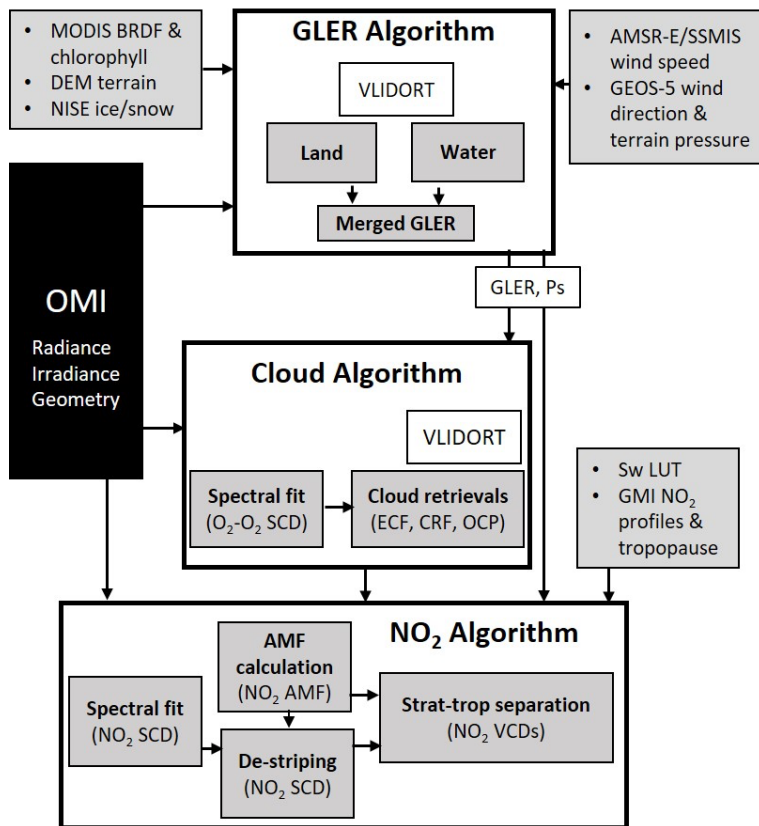
1290

Figure 1: Schematic diagram of the NASA OMI NO_2 algorithm, version 4.0, which is coupled with the cloud and geometry-dependent surface Lambertian Equivalent Reflectivity (GLER) algorithms that ultimately produces stratospheric (strat) and tropospheric (trop) NO_2 vertical column densities (VCDs). Acronyms used here are described in relevant sections below. VLIDORT: Vector Linearized Discrete Ordinate Radiative Transfer; MODIS: Moderate

1296 Resolution Imaging Spectro-radiometer; BRDF: bidirectional reflectance distribution function;
1297 DEM: Digital Elevation Model; NISE: Near-real-time Ice and Snow Extent; AMSR-E: Advanced
1298 Microwave Scanning Radiometer for Earth Observing System (EOS); SSMIS: Special Sensor
1299 Microwave Imager / Sounder; GEOS-5: Goddard Earth Observing System, Version 5; Ps: surface
1300 (terrain) pressure over OMI pixel; ECF: Effective Cloud Fraction; CRF: Cloud Radiance Fraction;
1301 OCP: Optical Centroid Pressure; Sw: Scattering weight; LUT: Look-up table GMI: Global
1302 Modeling Initiative; AMF: Air Mass Factor; SCD: Slant Column Density.

1303
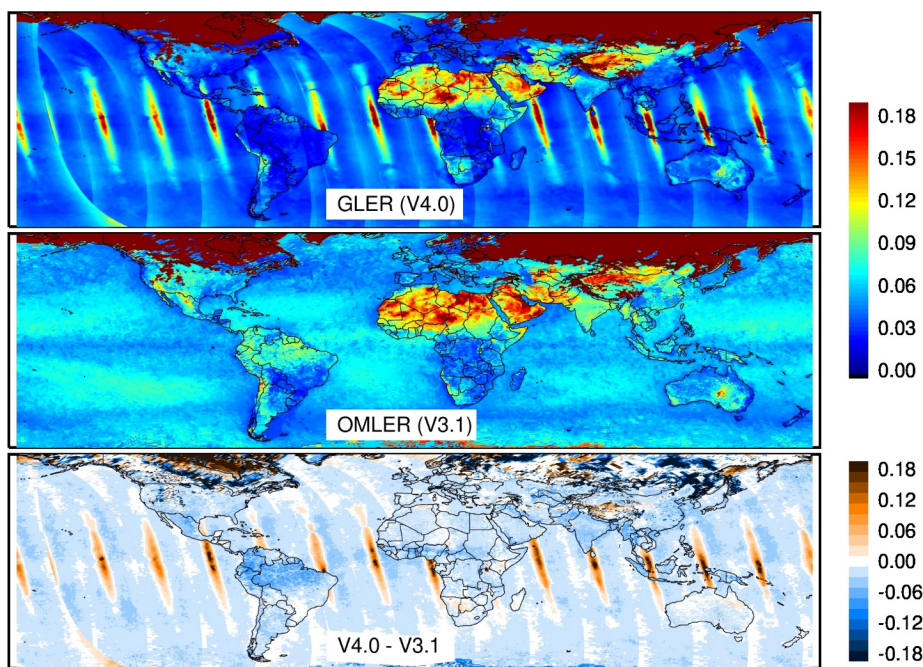
1304

1305 **Figure 2**: Surface reflectivity at 440 nm (top) derived using MODIS BRDF data with OMI
1306 geometry (GLER) on March 20, 2005 compared with (middle) OMI-based monthly LER
1307 climatology (OMLER) for the month of March (Kleipool et al., 2008). The bottom panel shows
1308 the difference between MODIS-based and climatological surface reflectivity data.
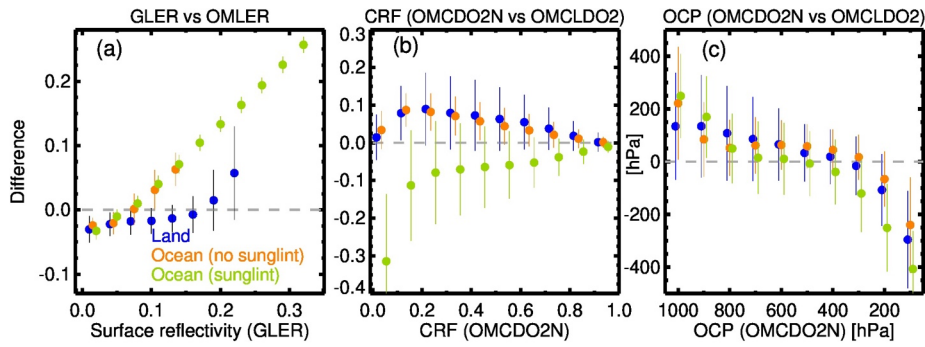
1309

Figure 3: Differences (V4.0 – V3.1) in (a) surface reflectivity, (b) cloud radiance fraction, and (c) cloud optical centroid pressure for March 20, 2005, as used in V3.1 and V4.0 algorithms and binned by the values of corresponding parameters from V4.0. Data are separated for land (blue) and ocean surfaces, and by sunglint (green) and non-sunglint (orange) geometry over ocean. The vertical bars represent the standard deviation for each bin of those parameters.

1315
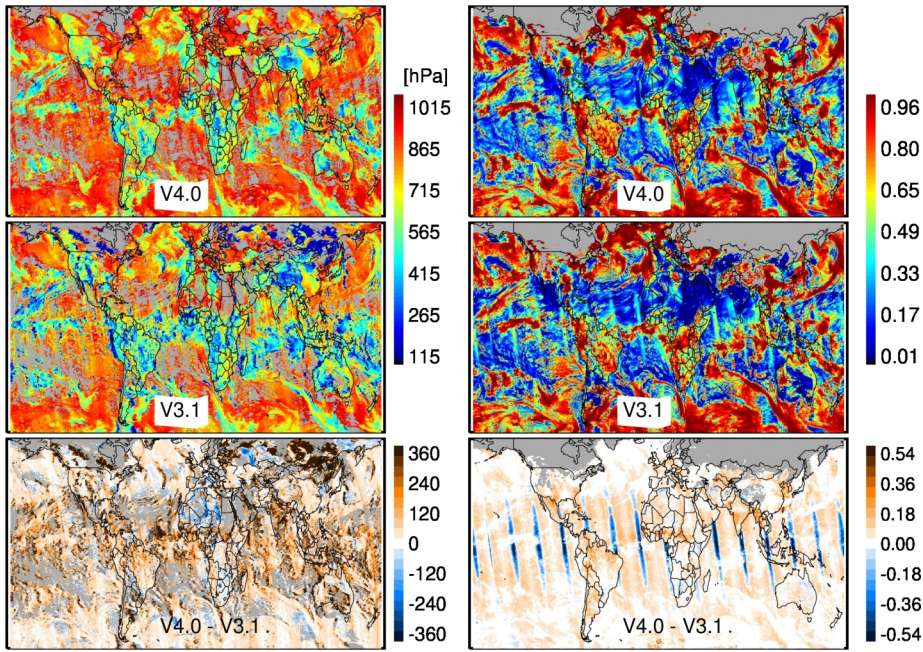
1316

Figure 4: Cloud optical centroid pressure at 477 nm (left) and cloud radiance fraction at 440 nm (right) retrieved for March 20, 2005 with OMNO2 V4.0 (top) and V3.1 (middle) algorithms, respectively. The bottom rows show their differences. The gray color represents the OMI pixels with retrieved cloud pressure equal to terrain pressure in V4.0 on the left and over snow/ice surface identified by the NISE flag on the right.
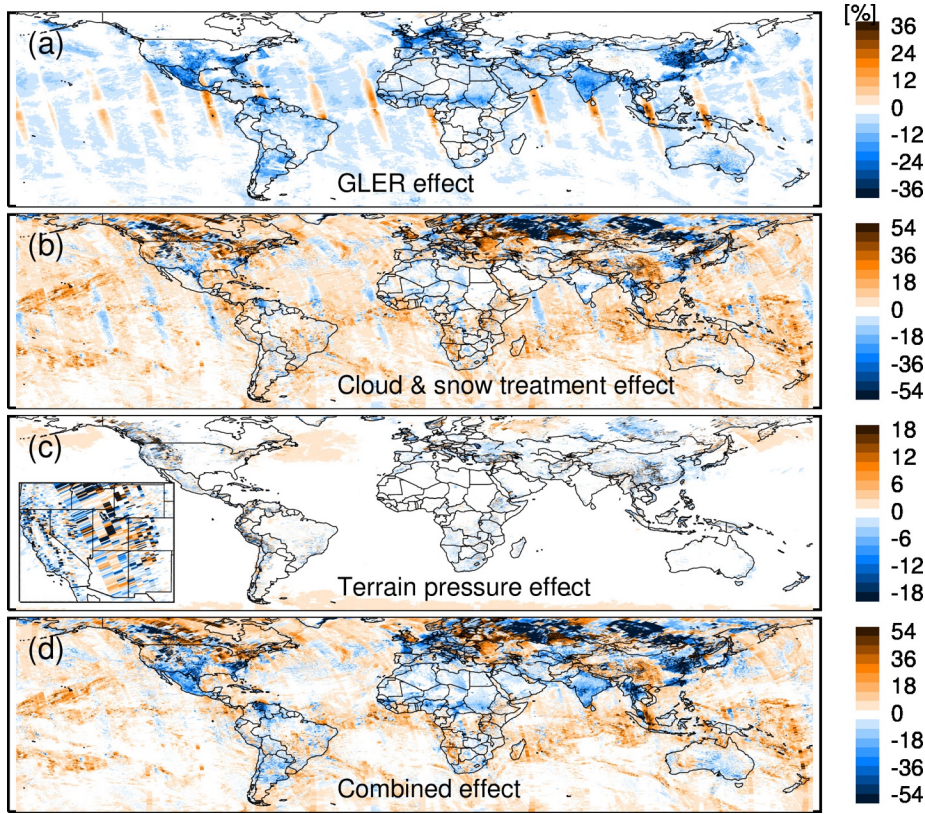
1322

Figure 5: Impact on tropospheric AMF (i.e., V4.0 – V3.1) from changes in (a) surface reflectivity, (b) cloud and surface treatment, (c) terrain pressure, and (d) their combination on March 20, 2005. The figure 5(c) inset shows zoomed view of impact over complex terrain in the western US.
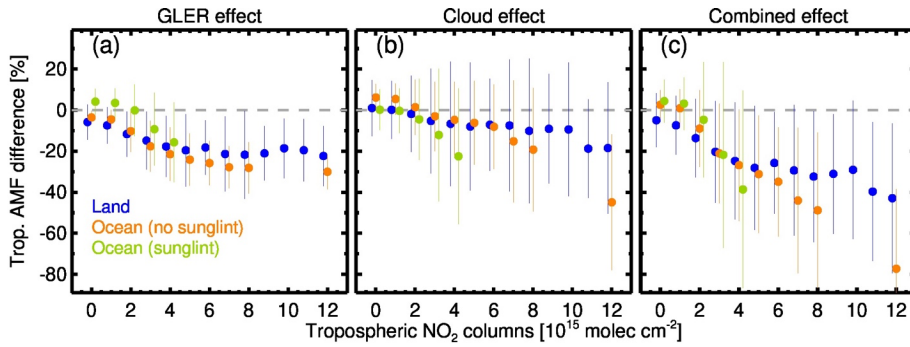
1326

Figure 6: The impact on tropospheric AMF (i.e., V4.0 – V3.1) from changes in (a) surface
reflectivity, (b) cloud, and (c) their combination for clear and partially cloudy scenes (CRF<0.5)
on March 20, 2005. Percent differences in tropospheric AMF are sorted by tropospheric NO_2
columns, separating them by land (blue) and ocean, and by sunglint (green) and non-sunglint
(orange) geometry over ocean. The vertical bars represent the standard deviations for the
tropospheric NO_2 column bins.

1333

1334

1335

1336
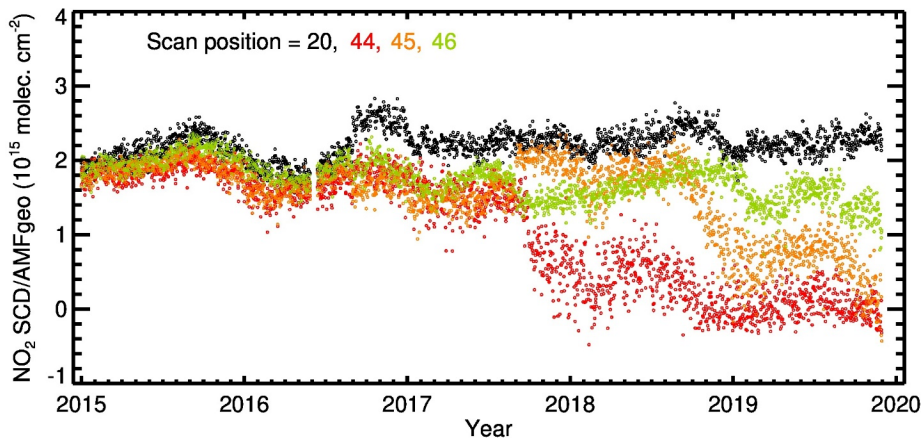
1337

Figure 7: The time series of OMI NO_2 SCD normalized by the geometric AMF for clear-sky and
1338
partially cloudy conditions (CRF<0.5) over the Pacific Ocean. The data are separated by cross-
1339
track scan position, comparing the presumably RA-free row 20 (black) with rows 44 (red), 45
1340
(orange), and 46 (green). The row numbers are 0-based.
1341

1342
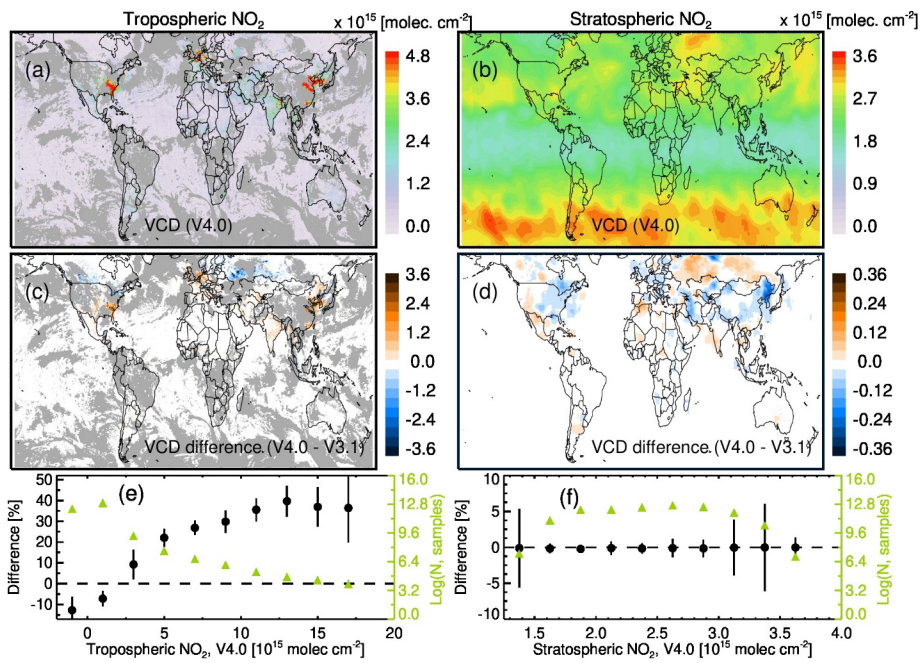
1343

Figure 8: Tropospheric (a) and stratospheric (b) NO$_2$ VCD from V4.0 and their differences (c, d)
1344
with V3.1 data (V4.0 – V3.1) for March 20, 2005. The gray color in the tropospheric NO$_2$ maps
1345
represent cloudy areas (CRF>0.5). Bottom panels show average (black circles) and standard error
1346
(vertical bars) of the relative difference, $100 \times (V4.0 – V3.1)/V3.1$, for tropospheric (e) and
1347
stratospheric (f) NO$_2$ VCDs plotted as a function of respective NO$_2$ column amounts. The green
1348
symbols represent the logarithm of the number of samples.
1349
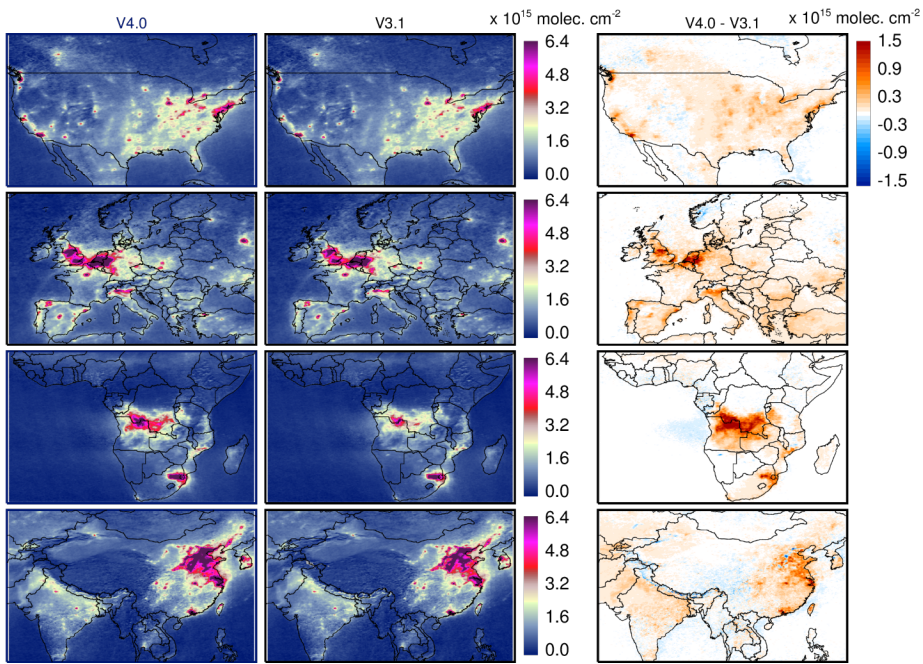
1350

Figure 9: Three-month (June, July, August) average tropospheric NO₂ columns for low cloud
conditions (CRF<0.5) in 2005 over North America (1st row), Europe (2nd row), southern Africa
(3rd row), and Asia (4th row) from V4.0 (1st column), V3.1 (2nd column), and their difference (V4.0
– V3.1).
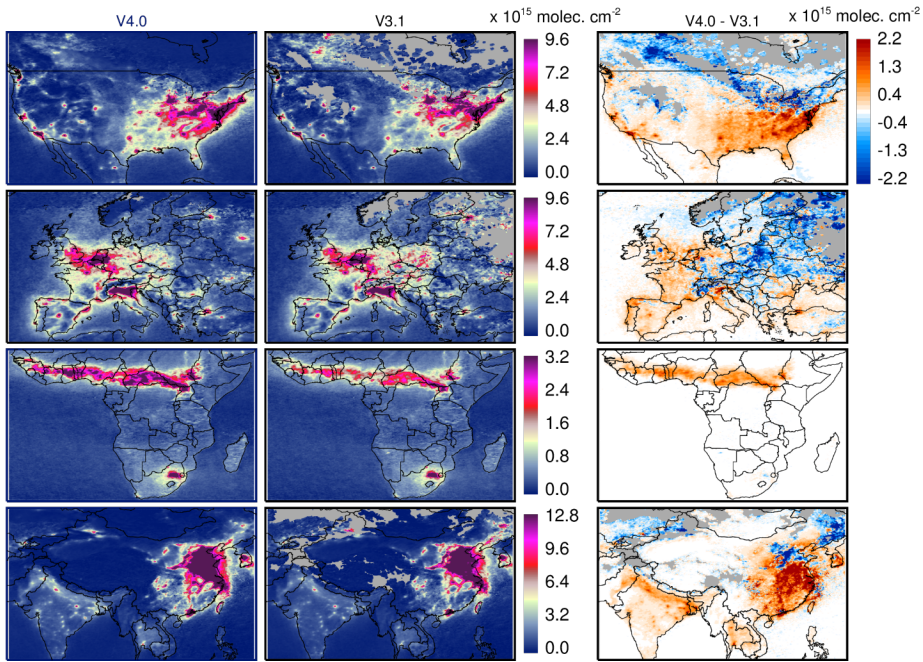
Figure 10: Same as Figure 9, but for December, January, and February. The gray areas represent a lack of good observations as determined by data quality flags.

1371
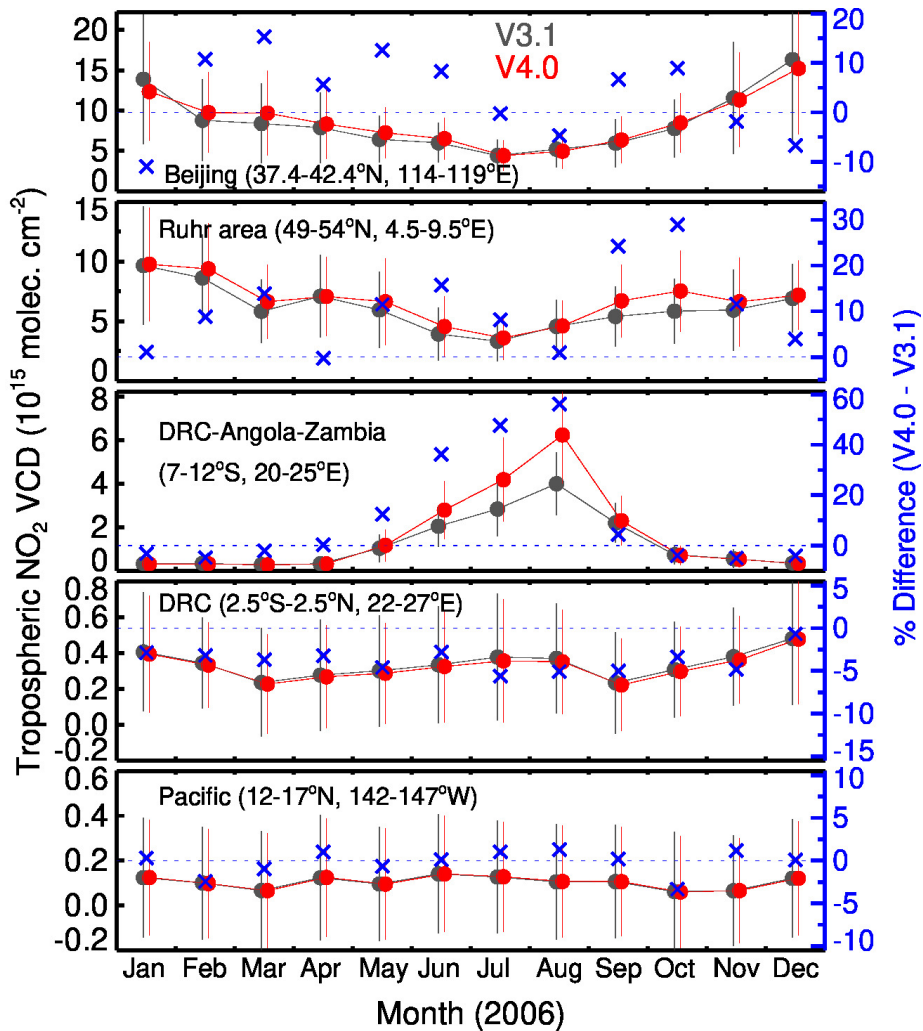
Figure 11: Monthly average tropospheric NO₂ columns in 2006 calculated from V3.1 (black)

1373   and V4.0 (red) data over selected 5º latitude × 5º longitude boxes from locations that are

1374   dominated by either anthropogenic (Beijing, China and Ruhr area, Germany), biomass burning

1375   (Democratic Republic of Congo (DRC), Angola, and Zambia), lightning (DRC), or no significant

1376   (Pacific) NOₓ sources. The vertical bars show the monthly standard deviation. The blue symbols

1377   that correspond to the right y-axis show monthly relative difference (in percent) between V4.0

1378   and V3.1.
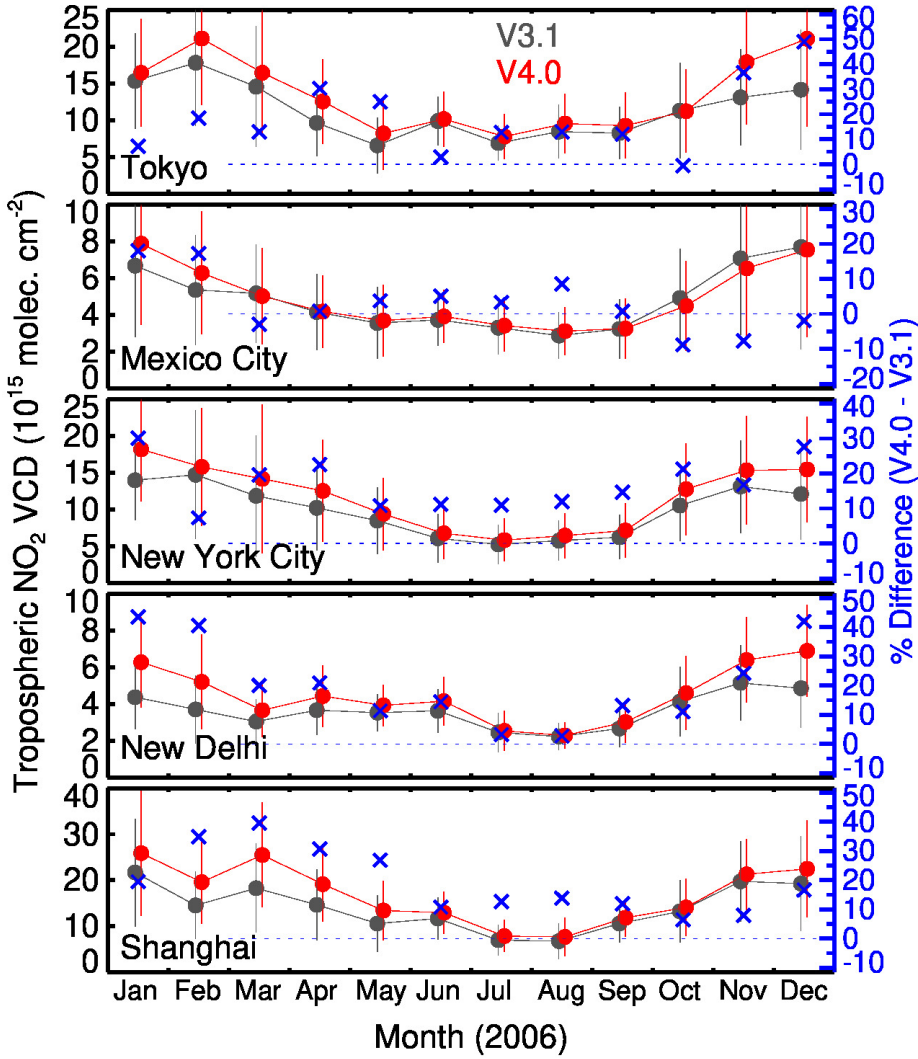
1379

Figure 12: Same as Figure 11, but for 1º latitude × 1º longitude wide box over the five highly

1381   populated and polluted cities.

1382

1383

1384
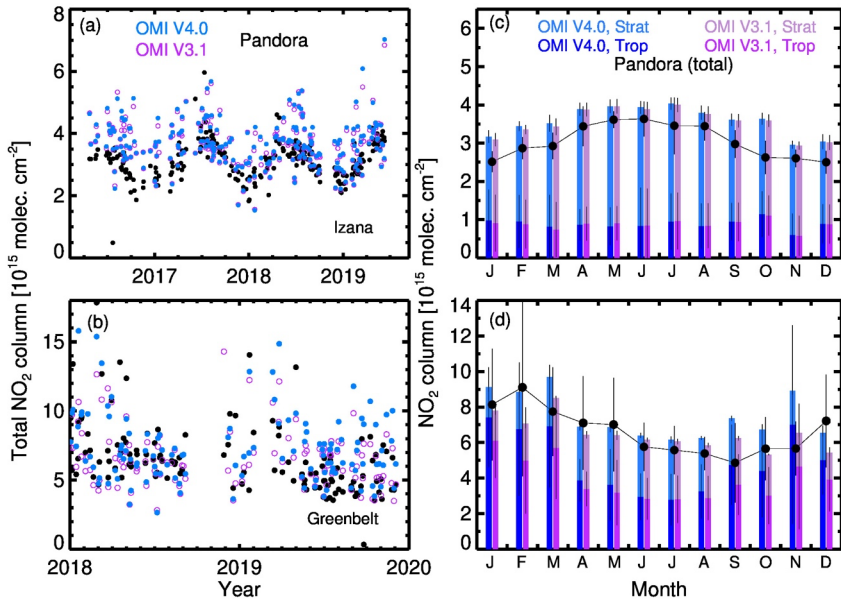
1385

1386 **Figure 13**: The time series of NO$_2$ total columns retrieved from Pandora (black circles) and OMI

1387 at (a) Izaña, Spain and (b) Greenbelt, Maryland, USA, with the OMI retrievals represented by the

1388 filled blue (V4.0) and open purple (V3.1) circles. Right panels show monthly variation of NO$_2$

1389 total columns at (c) Izaña for 2016–2019 and (d) Greenbelt for 2018-2019, as calculated from

1390 Pandora (black line with filled circles) and OMI measurements (bars). OMI NO$_2$ total columns

1391 retrieved with V4.0 (blue) and V3.1 (purple) are separated into tropospheric and stratospheric

1392 components. The vertical lines represent the standard deviation from the average.

1393
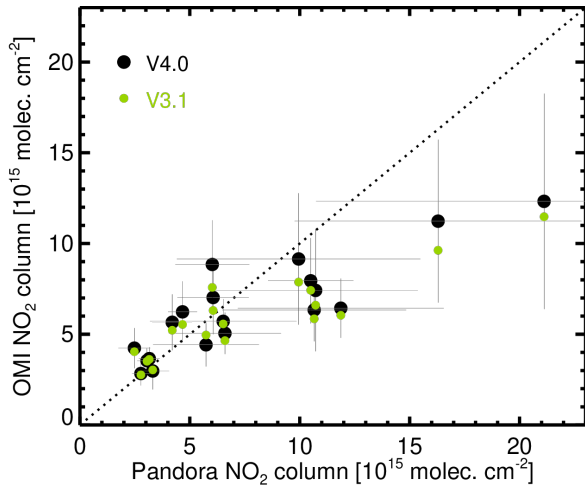
1394

1395 **Figure 14**: The scatter plot of Pandora versus OMI V4.0 (black) and V3.1 (green) average total

1396 column NO_2 for 18 Pandora sites. The vertical and horizontal lines represent the standard

1397 deviations for Pandora and OMI, respectively. The dotted line represents the 1:1 relationship.

1398
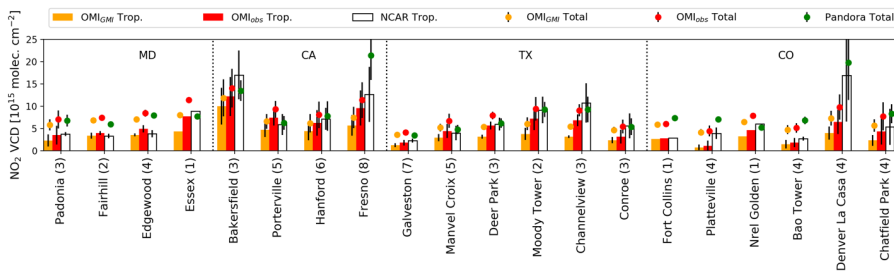
1399

1400 **Figure 15**: Site average total (circles) and tropospheric (bars) NO_2 column data from P-3B spiral

1401 (white bars), Pandora (green circles), and OMI (orange and red). The OMI tropospheric columns

1402   are derived using GMI-simulated (OMI$_{GMI}$, orange) and P-3B (OMI$_{obs}$, red) NO$_2$ profiles. The

1403   vertical bars for sites with over 2 observations represent the standard deviations.

1404

1405   **Table 1**. Summary of algorithms and approaches used in the NASA NO$_2$ algorithms versions 3.1 and 4.0

Algorithm Component		Version 3.1 (Released 2018)	Version 4.0 (Released 2019)
Spectral fit	NO$_2$	Modified DOAS fit (Marchenko et al, 2015)	Same as in V3.1
	O$_2$-O$_2$	DOAS fit from KNMI (Veefkind et al, 2016)	Modified DOAS fit (Vasilkov et al, 2018)
AMF	Terrain reflectivity	Monthly climatology (Kleipool et al., 2008)	Daily GLER data (Vasilkov et al., 2017; Qin et al., 2019; Fasnacht et al., 2019)
	Terrain pressure	At pixel center (calculated from terrain height and GMI terrain pressure)	Average over pixel (calculated from terrain height and GMI terrain pressure)
	Cloud pressure and fraction	Operational O$_2$-O$_2$ cloud product (OMCLDO2) v2.0 (Veefkind et al., 2016)	New O$_2$-O$_2$ cloud product (OMCDO2N) derived using the GLER product (Vasilkov et al., 2018)
	Cloud radiance fraction	Calculated at 440 nm from OMCLDO2 v2.0 cloud fraction using VLIDORT-based look-up-table	Calculated at 440 nm from OMCDO2N cloud fraction using VLIDORT-based look-up-table
	Scattering weights	TOMRAD-based look-up table	Same as in V3.1
	A-priori NO$_2$ profiles	GMI-derived yearly varying monthly mean profiles at 1°×1.25°	Same as in V3.1
Stripe correction		Based on data from 30°S - 5°N of 5 orbits	Same as in V3.1
Stratosphere-troposphere separation		Spatial filtering and interpolation (Bucsela et al., 2013), but with minor changes in box sizes	Same as in V3.1

1406

1407

1408

1409

1410

Table 2: Comparison of OMI V3.1 and V4.0 NO$_2$ retrievals based on a priori NO$_2$ profiles from GMI (OMI) and P-3B aircraft observations (OMI$_{obs}$) with P-3B observations during the DISCOVER-AQ field campaign. Shown here are correlation coefficient (r) and mean difference, which is calculated as OMI minus validation data.

Campaign locations	V3.1				V4.0			
	OMI vs P-3B		OMI$_{obs}$ vs P-3B		OMI vs P-3B		OMI$_{obs}$ vs P-3B	
	Mean diff. (%)	r	Mean diff. (%)	r	Mean diff. (%)	r	Mean diff. (%)	r
Maryland	-40.7	0.39	-23.7	0.61	-33.9	0.40	-5.0	0.69
California	-53.8	0.77	-42.4	0.73	-44.6	0.81	-18.7	0.83
Texas	-54.9	0.65	-25.5	0.82	-53.7	0.68	-18.8	0.85
Colorado	-67.5	0.73	-54.2	0.70	-66.2	0.70	-45.4	0.70
All	-55.5	0.75	-38.8	0.74	-50.3	0.74	-23.1	0.79

Table 3: Same as Table 2, but with Pandora NO$_2$ column observations.

Campaign locations	V3.1				V4.0			
	OMI vs Pandora		OMI$_{obs}$ vs Pandora		OMI vs Pandora		OMI$_{obs}$ vs Pandora	
	Mean diff. (%)	r	Mean diff. (%)	r	Mean diff. (%)	r	Mean diff. (%)	r
Maryland	-21.8	0.21	2.4	0.30	-13.0	0.13	25.6	0.27
California	-58.5	0.24	-47.9	0.20	-49.8	0.33	-24.6	0.49
Texas	-26.9	0.65	21.6	0.81	-25.3	0.67	31.7	0.81
Colorado	-68.2	0.72	-55.2	0.69	-67.6	0.70	-46.7	0.65
All	-52.3	0.53	-33.5	0.47	-46.9	0.56	-16.3	0.63

Deleted: V4.0

Deleted: and Pandora column